Alma Mater Studiorum · Università di Bologna

Scuola di Scienze
Dipartimento di Fisica e Astronomia
Corso di Laurea Magistrale in Fisica

Measure of the branching ratio of the $B^0 \to D^{*-}\tau^+\nu_\tau$ decay at LHCb: a preliminary study for $R_{D^*}\left(q^2\right)$ in 3-prong τ decays

Relatore:
Prof. Angelo Carbone

Correlatore:
Dott. Federico Betti

Presentata da:
Daniele Manuzzi

Anno Accademico 2016/2017

Abstract

Ad oggi non sono state ancora osservate differenze significative tra i risultati sperimentali e le previsioni teoriche del Modello Standard. Tuttavia esistono delle differenze che potrebbero indicare l'esistenza di Nuova Fisica. Tre queste una delle principali riguarda: $\mathcal{R}_{D^*} = \mathcal{B}(B^0 \to D^{*-}\tau^+\nu_\tau)/\mathcal{B}(B^0 \to D^{*-}\mu^+\nu_\mu)$ e $\mathcal{R}_D\mathcal{B}(B^0 \to D^-\tau^+\nu_\tau)/\mathcal{B}(B^0 \to D^-\mu^+\nu_\mu)$. Questi rapporti sono stati misurati dagli esperimenti *BaBar* [1] e *Belle* [2] ed anche dall'esperimento LHCb [3]. Al momento la combinazione di tutti questi risultati [4] si discosta di 3.9 σ dalle previsioni teoriche basate sul Modello Standard [5]. Se questa deviazione fosse confermata da future misure più precise, rappresenterebbe una evidenza indiretta dell'esistenza di una nuova dinamica. Recentemente LHCb ha realizzato la misura di $\mathcal{R}_{D^*}$ utilizzando un ulteriore canale di decadimento del tauone: $\tau^+ \to \pi^+\pi^-\pi^+(\pi^0)\bar{\nu}_\tau$. Infatti la precedente misura era stata realizzata utilizzando il decadimento semi-leptonico del tau. Il lavoro di tesi presentato in questo documento riguarda lo studio preliminare di fattibilità della misura di $\mathcal{R}_{D^*}$ in regioni di $q^2 = (p_{B^0} - p_{D^{*-}})^2$, mediante il decadimento $B^0 \to D^{*-}\tau^+(\to 3\pi\pi^0\bar{\nu}_\tau)\nu_\tau$. Il campione di dati utilizzato corrisponde a quelli raccolti da LHCb durante il RUN-1 e quindi pari a 3 fb^{-1} di luminosità integrata. Questo lavoro ha permesso di concludere che questo tipo di analisi è fattibile, nonostante il piccolo numero di eventi di segnale osservati. Tuttavia per rendere l'analisi pronta per la pubblicazione, diversi studi, inclusi quelli degli effetti sistematici, sono ancora necessari.

Contents

Introduction

Since the original formulation of quark mixing [6], the flavour structure of the Standard Model (SM) has been experimentally tested and well established [4, 7]. At the same time, the theoretical community managed to go well beyond leading order computations [8]. With the latest results, LHCb achieved an unprecedented precision in several tests of the SM, in particular the LHCb Collaboration measured the ratio [9]

$$R_K \equiv \frac{\mathcal{B}(B^+ \to K^+\mu^+\mu^-)}{\mathcal{B}(B^+ \to K^+e^+e^-)} = 0.745^{+0.090}_{-0.074}(\text{stat}) \pm 0.036(\text{syst}). \tag{1}$$

This result is 2.4 σ below the SM expectation [10]. Moreover, the SM prediction for $\mathcal{B}(B^+ \to K^+\mu^+\mu^-)$ was found 45% higher than the experimental results [11]. Observables related to this kind of decay seem particularly interesting, because directly testing FCNC, which are strongly suppressed within the SM.

The LHCb results for R_K have attracted theoretical attention and many models [12] have proposed the existence of particles, at or above 1 TeV, which may induce new and non-universal lepton interactions. However, "any departure from lepton flavour universality (LFUV) is necessarily associated with the violation of family lepton number conservation. No known symmetry principle can protect the one in the absence of the other" [12].

Currently other related hot field of research for the search of LFUV, involve the Flavour Changing Charged Current decay $b \to c\ell\nu_\ell$. In this case, several hadronisation schemes are possible, *e.g.* $B \to X_c\ell\nu_\ell$ with $X_c = D^*, D^0, D^+, D_s, \Lambda_c, J/\Psi$ and $\ell = e, \mu, \tau$. All of them share nice common features as precise SM prediction and branching fraction much bigger than the value reported in equation (1). Furthermore, the cited charmed states have different spin properties, which may make them sensitive to different underlying processes. On the other hand, reconstruction and statistical analysis are make difficult by the ν_ℓ presence; when $\ell = \tau$ even two neutrinos are necessarily involved in event reconstruction because in general the tau decays inside the detectors.
So far the ratio of the branching fractions

$$\mathcal{R}_{D^{(*)}} = \frac{\mathcal{B}(\bar{B}^0 \to D^{(*)+}\tau^-\bar{\nu}_\tau)}{\mathcal{B}(\bar{B}^0 \to D^{(*)+}\mu^-\bar{\nu}_\mu)}, \tag{2}$$

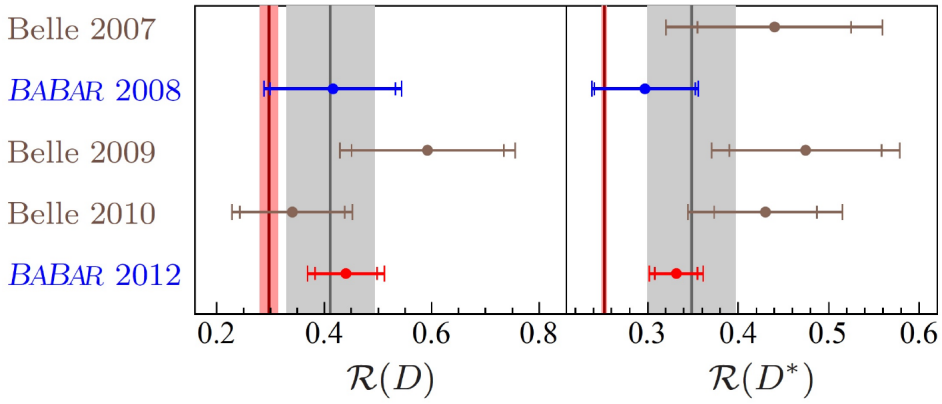

Figure 1: Results of $\mathcal{R}_D$ and $\mathcal{R}_{D^*}$ measurements performed by BaBar and Belle from 2007 to 2012. The vertical bands represent the average of the measurements without the before BaBar 2012 one (light shading) and the the SM predictions (dark shading). The widths of the bands represents the uncertainties.

have been repeatedly measured by the BaBar and Belle collaborations (Fig. 1). Recently also the LHCb collaboration performed a measurement of $\mathcal{R}_{D^*}$ [3] with Run-1 data. Its combination with last results by BaBar [1] and Belle [2] is graphically displayed in Fig. 2. The total discrepancy with the SM reaches about 4 σ, strongly requiring further inquiry.

In order to improve the experimental precision the LHCb Collaboration decided to exploit the hadronic tau decay $\tau^- \to \pi^-\pi^+\pi^-\nu_\tau$, which were not included in his previous analysis. Its main feature is a final state composed of multiple charged particles. That permits to reconstruct the tau decay vertex. This can be used to overcome the lack of information caused by the undetectable neutrinos. The drawback is that LHC is a hadronic collider thus this kind of background could overwhelm the signal. To deal with that a complex analysis was built up: many ancillary studies were required to constrain estimations of backgrounds yields and to obtain better descriptions of their shapes. The final result[1]

$$\mathcal{R}_{D^*} = 0.285 \pm 0.019 \pm 0.025 \pm 0.013, \tag{3}$$

has been submitted Physical Review D [13]. This is however an integrated measurement, *i.e.* it takes into account all the allowed kinematic range. The SM is able to predict the dependence of $\mathcal{R}_{D^*}$ on the square of the transferred 4-momentum, namely $q^2 = (p_{B^0} - p_{D^*})^2$. New Physics phenomena, suppressed in the integral, may appear as enhanced analysing $\mathcal{R}_{D^*}$ in smaller ranges of q^2. This step requires detailed studies due to the fact that sub-ranges mean less statistic (larger uncertainties). Moreover this kind of analysis requires to perform a study based on observables and variables not correlated with q^2.

[1]The uncertainties reported are statistical, systematic and due to external input, respectively.

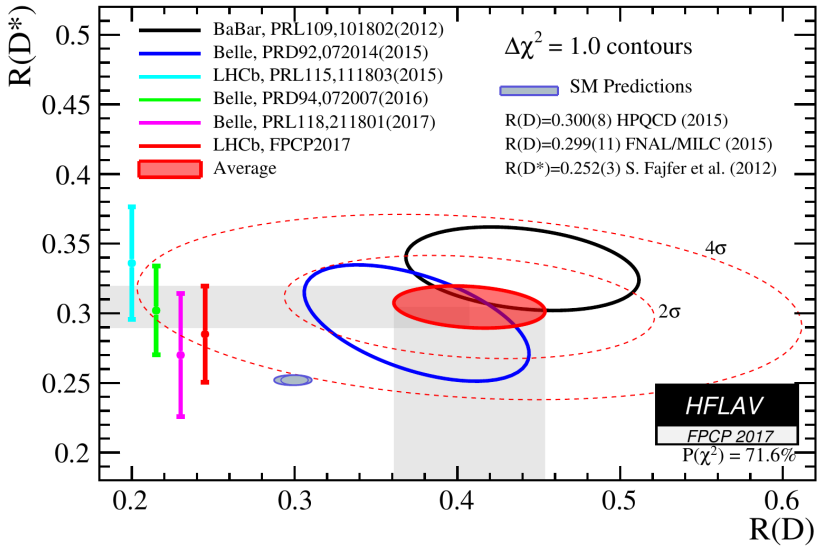

Figure 2: Average of $\mathcal{R}_{D^*}$ vs. $\mathcal{R}_D$. The cyan band is the LHCb measurement, the black and blue ellipses represent the BaBar and Belle measurements, respectively. The green and magenta bands represent new measurements presented by BELLE in 2016. The red ellipse is the average of all measurements, to be compared with the SM prediction in blue-gray.

The thesis is organised as follow: Chapter 1 introduces the flavour and the lepton universality within the SM. Chapter 2 reports the SM prediction for $\mathcal{R}_{D^*}$ and briefly introduces the formalism of "effective theories". Chapter 3 reported the main features of LHCb detector. Chapter 4 describes in detail the analysis which measures the yield for $B^0 \to D^{*-}\tau^+\nu_\tau$. Finally, 5 accounts for the preliminary studies conducted to test the feasibility of a $\mathcal{R}_{D^*}$ measure in two different q^2 sub-ranges.

Chapter 1

Standard Model and Flavour Universality

In particle physics, the term *flavor* describes several copies of the same gauge representation, namely several fields, that are assigned the same quantum charges [14]. Within the Standard Model (SM), there are four different kind of particles, each coming in three flavours:

- up-like quarks: u, c, t;
- down-like quark: d, s, b;
- charged leptons: e, μ, τ;
- neutrinos: ν_e, ν_μ, ν_τ.

These are the rows of the fermionic part of the scheme displayed in Fig. 1.1. Columns, instead, identify three families (or generations) of quarks and three families of leptons; so each family includes two flavours[1].

Flavour physics studies interactions that distinguish between flavours. In the SM, interactions associated to unbroken gauge symmetries, therefore mediated by massless gauge bosons, do not distinguish among flavours, by definition. On the contrary, weak and yukawa interactions are the realm of flavour physics.

Flavour is mathematically encoded by parameters equipped with related indices (*flavour parameters*). In the SM there are thirteen of them: nine masses of the charged leptons and four (three angles and one phase) that rule the interactions of the charged weak-force carriers ($W^\pm$) with quark pairs.

Other remarkable definitions are:

[1] Some authors use different definitions of flavour [15–17]; we refer to [14, 18].

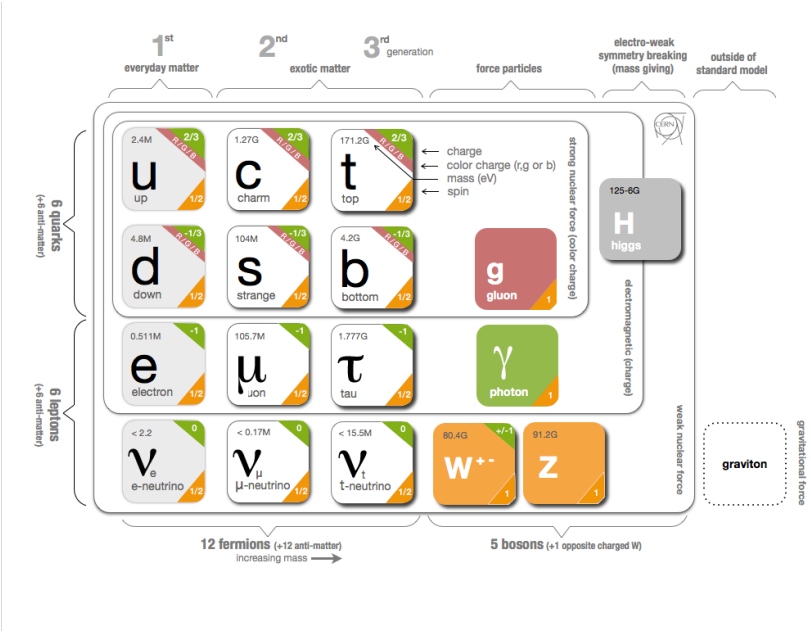

Figure 1.1: Scheme of elementary particles.

- **flavour universal** (or flavour-blind), which refers to interactions with couplings (or to parameters) that are proportional to the unit matrix in flavour spaces;
- **flavour diagonal**, which refers to interactions with couplings (or to parameters) that are diagonal, but not necessarily universal, in the flavour spaces;
- **flavour changing**, which refers to processes where the initial and final flavour-numbers (*i.e.*, the number of particles of a certain flavour minus the number of anti-particles of the same flavor) are different.

The goal of the rest of this section will be to analyse and clarify these concepts.

1.1 Genesis of Weak Universality

Leptons are coupled by the weak interaction (WI). A very first question is weather all this coupling depends in some way on flavour or not. To answer, $e-\mu$ pair can be tested by comparison of these decays of τ lepton:

$$\tau^- \to e^- \bar{\nu}_e \nu_\tau; \qquad \tau^- \to \mu^- \bar{\nu}_\mu \nu_\tau.$$

Not mentioning constants that are the same for both, the two partial widths [15] are:

$$\Gamma(\tau^- \to e^- \bar{\nu}_e \nu_\tau) \propto \frac{g_\tau^2}{M_W^2} \frac{g_e^2}{M_W^2} m_\tau^5; \quad \Gamma(\tau^- \to \mu^- \bar{\nu}_\mu \nu_\tau) \propto \frac{g_\tau^2}{M_W^2} \frac{g_\mu^2}{M_W^2} m_\tau^5, \tag{1.1}$$

where: M_W is the mass of the W boson, g_e, g_μ, g_τ indicate the *weak charge* of each lepton.

The ratio between the two widths can be estimated, measuring the two branching ratios:

$$\frac{\Gamma(\tau^- \to \mu^- \bar{\nu}_\mu \nu_\tau)}{\Gamma(\tau^- \to e^- \bar{\nu}_e \nu_\tau)} = \frac{\mathcal{B}(\tau^- \to \mu^- \bar{\nu}_\mu \nu_\tau)}{\mathcal{B}(\tau^- \to e^- \bar{\nu}_e \nu_\tau)} = \frac{g_\mu^2}{g_e^2} \frac{\rho_\mu}{\rho_e}, \tag{1.2}$$

where the last factor is the ratio between the two phase-space terms, which is exactly calculable from the kinematic theory. Results reported in [15] give:

$$\frac{\mathcal{B}(\tau^- \to \mu^- \bar{\nu}_\mu \nu_\tau)}{\mathcal{B}(\tau^- \to e^- \bar{\nu}_e \nu_\tau)} = \frac{(17.36 \pm 0.05)\%}{(17.84 \pm 0.05)\%} = 0.973 \pm 0.004, \tag{1.3}$$

that brings to:

$$\boxed{\frac{g_\mu}{g_e} = 1.003 \pm 0.002.} \tag{1.4}$$

The $\mu - \tau$ case can be checked considering their beta decay rates. In fact, assumed in first approximation that 100% of the muons decay in this channel, we can write:

$$\frac{\Gamma(\mu^- \to e^- \bar{\nu}_e \nu_\mu)}{\Gamma(\tau^- \to e^- \bar{\nu}_e \nu_\tau)} = \frac{1}{\tau_\mu} \frac{\tau_\tau}{\mathcal{B}(\tau^- \to e^- \bar{\nu}_e \nu_\tau)}, \tag{1.5}$$

where τ_μ and τ_τ are the mean lifetimes of the leptons. Moreover, from the theoretical point of view, we get:

$$\frac{\Gamma(\mu^- \to e^- \bar{\nu}_e \nu_\mu)}{\Gamma(\tau^- \to e^- \bar{\nu}_e \nu_\tau)} = \frac{g_e^2 g_\mu^2 m_\mu^5 \rho_\mu}{g_e^2 g_\tau^2 m_\tau^5 \rho_\tau}, \tag{1.6}$$

and then

$$\frac{g_\mu^2}{g_\tau^2} = \frac{1}{\tau_\mu} \frac{\tau_\tau}{\mathcal{B}(\tau^- \to e^- \bar{\nu}_e \nu_\tau)} \frac{m_\tau^5 \rho_\tau}{m_\mu^5 \rho_\mu}, \tag{1.7}$$

so it is necessary to measure two lifetimes, two masses and a branching ratio. In conclusion, substituting measurements [15], we get:

$$\boxed{\frac{g_\mu}{g_\tau} = 1.001 \pm 0.003.} \tag{1.8}$$

These calculation suggest the idea that the flavour of the involved leptons does not affect the intensity of the WI. At the same time, though, these transitions act on flavour, which changes between the initial an the final state. The same ideas, however, can not be naively applied to other interactions and to quarks. In fact, beyond WI, no *flavour changing* decays has ever been observed, yet. Moreover WI seems completely non-universal about quarks. For example, $\mathcal{B}(\Sigma^- \to n e^- \bar{\nu}_e) \sim 10^{-3}$, while $\mathcal{B}(\Sigma^+ \to n e^+ \nu_e) \sim 10^{-6}$ [19]. Furthermore, Fermi theory properly predicts lifetimes of neutrons

end pions, while for kaons it calculates a 20 times higher rate than the observed one [19]. Historically, the concept of *strangeness* (an so of flavour of the hadrons) was born, actually, to account for particles with oddly suppressed decay rates. One of the firstly proposed solution was, indeed, that strange particles are linked to a much more smaller Fermi constant than the one linked to strangeless particles.
Next sections will clarify the notions of flavour and universality, showing that the latter concept can be somehow recovered also for quarks.

1.2 Flavour in the Electroweak Model

Generalities. Flavour is a key point of the model proposed in the 60s by Glashow, Weinberg and Salam (GWS), to unify the description of electromagnetic and weak interactions within the SM [20–22]. In order to include weak charged currents (CC), this theory has to account for the following facts, concerning leptons:

i) CC have a $V - A$ structure;

ii) CC couple only leptons of the same family;

Therefore, Electroweak theory disposes the left-handed projection (i) of leptonic spinors in doublets (ii), imposing local gauge symmetry for the group $SU(2)_L$. In some way, the idea is to develop a sort of Yang-Mills theory for eigenstates of specified chirality (from this the subscript L); so each chiral eigenstate is equipped with new the quantum numbers of *weak isospin* (I).

Anyway, more is necessary to properly describe:

iii) electromagnetic (EM) and weak neutral currents (NS);

iv) interactions of right-handed leptons;

v) massless and always left-handed neutrinos; massless photon;

GWS model choices[2] to set up right-handed spinors in singlets, imposing $\nu_R = 0$. In this regard, leptonic multiplets notation is condensed here:

LEPTONS				
doublets	$\begin{pmatrix}\nu_{eL}\\ e_L\end{pmatrix}$	$\begin{pmatrix}\nu_{\mu L}\\ \mu_L\end{pmatrix}$	$\begin{pmatrix}\nu_{\tau L}\\ \tau_L\end{pmatrix}$	L_L^f
singlets	e_R	μ_R	τ_R	E_R^f

[2] In the following we will refer to [16] and [23] for notation and for not mentioned theoretical background.

Fields	I_3	Y	Q
ν_{eL}, $\nu_{\mu L}$, $\nu_{\tau L}$	$+1/2$	-1	0
e_L, μ_L, τ_L	$-1/2$	-1	-1
e_R, μ_R, τ_R	0	-2	-1
ϕ^+	$+1/2$	$+1$	$+1$
ϕ^0	$-1/2$	$+1$	0
u_L, c_L, t_L	$+1/2$	$+1/3$	$+2/3$
d_L, s_L, b_L	$-1/2$	$+1/3$	$-1/3$
u_R, c_R, t_R	0	$+4/3$	$+2/3$
d_R, s_R, b_R	0	$-2/3$	$-1/3$

Table 1.1: Quantum number assignation in GWS model.

where the last column economize the notation, namely $f = 1, 2, 3$ distinguish the various generations. Moreover, other ingredients need to be added to account for the above mentioned phenomenology. The first one is local gauge symmetry for the group $U(1)_Y$, whose quantum numbers Y are defined by a formula similar to Gell-Mann & Nishijima's one:

$$Q = I_3 + \frac{Y}{2}, \tag{1.9}$$

where Q is the electric charge and I_3 is the third component of weak isospin. Table 1.1 summarises quantum numbers assignation to chiral eigenstates.

These hypothesises imply the following covariant derivative:

$$D_\mu = \partial_\mu + igb_\mu^j \frac{\hat{\sigma}^j}{2} + ig'\mathcal{A}_\mu \frac{\hat{Y}}{2}, \tag{1.10}$$

where: $\mathcal{A}_\mu$ and b_μ^j $(j = 1, 2, 3)$ are the gauge fields needed to preserve $SU(2)_L \times U(1)_Y$ local gauge symmetry in the interaction lagrangian, g and g' are coupling constants, $\hat{Y}$ and $\hat{\sigma}^j/2$ are the operators, respectively, of weak hypercharge and weak isospin (essentially Pauli's matrices).

The total lagrangian of the electroweak theory can be written as:

$$\mathcal{L} = \mathcal{L}_B + \mathcal{L}_{\text{Higgs}} + \mathcal{L}_F + \mathcal{L}_{Yuk}, \tag{1.11}$$

here, $\mathcal{L}_B$ and $\mathcal{L}_{\text{Higgs}}$ describe free dynamics and mutual interactions between gauge bosons and Higgs boson. Instead $\mathcal{L}_F$ and $\mathcal{L}_{Yuk}$ introduce fermions and are both sum of two independent contributions: one from leptons, one from quarks.

Bosons

The known configuration of weak and electromagnetic vector bosons can be straightforwardly obtained, including Higgs sector and Spontaneous Symmetry Braking (SSB) [24–27]. Specifically, the Higgs field ϕ is a $SU(2)_L$ doublet:

$$\phi = \begin{pmatrix} \phi^+ \\ \phi^0 \end{pmatrix}, \tag{1.12}$$

with an assumed vacuum expectation value given by:

$$\langle 0 | \, \phi \, | 0 \rangle = \begin{pmatrix} 0 \\ v/\sqrt{2} \end{pmatrix}. \tag{1.13}$$

Fluctuations about this value can be parametrized by:

$$\phi = \begin{pmatrix} 0 \\ \frac{1}{\sqrt{2}}(v + H) \end{pmatrix}, \tag{1.14}$$

where H is the physical Higgs field. The interaction lagrangian can be written as:

$$\mathcal{L}_{\text{Higgs}} + \mathcal{L}_B = (D_\mu \phi)^\dagger (D_\mu \phi) + \tilde{\mu}^2 \phi^\dagger \phi - \frac{\lambda}{4}(\phi^\dagger \phi)^2 - \frac{1}{4} B^j_{\mu\nu} B^{\mu\nu}_j - \frac{1}{4} \mathcal{F}_{\mu\nu} \mathcal{F}_{\mu\nu}, \tag{1.15}$$

where $B^j_{\mu\nu}$ and $\mathcal{F}_{\mu\nu}$ are the field strength tensors respectively for $SU(2)$ and $U(1)$. Then, substituting (1.14), the lagrangian includes[3] the following terms:

$$\mathcal{L}_{\text{Higgs}} + \mathcal{L}_B \supset \tfrac{1}{2} \partial_\mu H \partial^\mu H + \tag{1.16}$$

$$- \frac{1}{2}(\partial_\mu W^+_\nu - \partial_\nu W^+_\mu)(\partial^\mu W^{-\nu} - \partial^\nu W^{+\mu}) + \tag{1.17}$$

$$- \frac{1}{4}(\partial_\mu Z_\nu - \partial_\nu Z_\mu)(\partial^\mu Z^\nu - \partial^\nu Z^\mu) + \tag{1.18}$$

$$- \frac{1}{4}(\partial_\mu A_\nu - \partial_\nu A_\mu)(\partial^\mu A^\nu - \partial^\nu A^\mu) + \tag{1.19}$$

$$- \tilde{\mu}^2 H^2 + g^2 \frac{v^2}{4} W^+_\mu W^{-\mu} + (g^2 + g'^2) \frac{v^2}{8} Z_\mu Z^\mu (+0 A_\mu A^\mu). \tag{1.20}$$

where gauge fields have been redefined to get the physical mass eigenstates:

$$W^\pm_\mu = \frac{1}{\sqrt{2}}(b^1_\mu \mp i b^2_\mu); \tag{1.21}$$

$$\begin{pmatrix} Z_\mu \\ A_\mu \end{pmatrix} = \begin{pmatrix} \cos\theta_W & -\sin\theta_W \\ \sin\theta_W & \cos\theta_W \end{pmatrix} \begin{pmatrix} b^3_\mu \\ a_\mu \end{pmatrix} \quad \text{with:} \quad \sin\theta_W = \frac{g}{\sqrt{g^2 + g'^2}}. \tag{1.22}$$

As a matter of fact, terms (1.16)-(1.19) evidently refer to the free dynamics of the bosonic fields. On the other hand, term (1.20) shows that EW theory properly predicts massive Higgs, W and Z fields, while photon, A, remains massless.

[3] For simplicity all interaction terms between gauge and Higgs fields are omitted.

Leptons

The EW interaction lagrangian for leptons is:

$$\mathcal{L}_F^l = \sum_{f=1}^{3} \bar{L}_L^f i\not{D}_\mu L_L^f + \bar{E}_R^f i\not{D}_\mu E_R^f, \tag{1.23}$$

which can instructively be rewritten in this way:

$$\mathcal{L}_F^l = \sum_f \bar{L}_L^f i\not{\partial}_\mu L_L^f + \bar{E}_R^f i\not{\partial}_\mu E_R^f + g J_j^{f\mu} b_\mu^j + g' J_Y^{f\mu} a_\mu, \tag{1.24}$$

being $J_j^{f\mu} = \bar{L}_L^f \gamma^\mu \frac{\hat{\sigma}_j}{2} L_L^f$ and $J_Y^{f\mu} = \bar{L}_L^f \gamma^\mu \frac{\hat{Y}}{2} L_L^f + \bar{E}_R^f \gamma^\mu \frac{\hat{Y}}{2} E_R^f$ the Noether's currents conserved because of $SU(2)_L$ and $U(1)_Y$ global symmetries, respectively.

From there, the usual distinction between CC, NC and EM currents soon reappears passing to mass eigenstates of gauge bosons, according to (1.21)-(1.22):

$$\mathcal{L}_F^l \supset \mathcal{L}_{\text{INT}}^l = \sum_f g J_j^{f\mu} b_\mu^j + g' J_Y^{f\mu} a_\mu = \mathcal{L}_{CC}^l + \mathcal{L}_{Neut.}^l, \tag{1.25}$$

with:

- $\mathcal{L}_{CC}^l = \sum_f g(J_1^{f\mu} b_\mu^1 + J_2^{f\mu} b_\mu^2) = \sum_f \frac{g}{\sqrt{2}}[J_+^{f\mu} W_\mu^- + J_-^{f\mu} W_\mu^+]$, where the charge changing currents are defined as $J_\pm^{f\mu} = J_1^{f\mu} \mp J_2^{f\mu}$; a more explicit expression is $J_-^{1\mu} = \bar{\nu}_{eL} \gamma^\mu e_L$. As a consequence, for the lagrangian we have[4]:

$$\mathcal{L}_{CC}^l = \frac{g}{\sqrt{2}} \left[\left(\bar{\nu}_e \gamma^\mu \tfrac{1-\gamma^5}{2} e + \bar{\nu}_\mu \gamma^\mu \tfrac{1-\gamma^5}{2} \mu + \bar{\nu}_\tau \gamma^\mu \tfrac{1-\gamma^5}{2} \tau \right) W_\mu^+ + h.c. \right] \tag{1.26}$$

- $\mathcal{L}_{Neut.}^l = \sum_f g J_\mu^{f3} b_3^\mu + g' J_Y^{f\mu} \mathcal{A}_\mu = -\sum_f g \sin\theta_W J_{EM}^{f\mu} A_\mu + \frac{g}{\cos\theta_W} J_{NC}^{f\mu} Z^\mu$. Here:

$$J_{EM}^{1\mu} = \bar{e_L} \gamma^\mu e_R + \bar{e_R} \gamma^\mu e_L;$$
$$J_{NC}^{1\mu} = \left(\sin^2\theta_W - \tfrac{1}{2}\right) \bar{e}_L \gamma^\mu e_L + (\sin^2\theta_W) \bar{e}_R \gamma^\mu e_R + \left(\tfrac{1}{2}\right) \bar{\nu}_{eL} \gamma^\mu \nu_{eL}.$$

  If $q = -g \sin\theta_W$, we get :

$$\mathcal{L}_{EM}^l = q(\bar{e}\gamma^\mu e + \bar{\mu}\gamma^\mu \mu + \bar{\tau}\gamma^\mu \tau) A^\mu; \tag{1.27}$$

  concerning weak neutral current, instead:

$$\mathcal{L}_{NC}^l = \frac{g}{\cos\theta_W} \sum_\ell \bar{\ell}\gamma^\mu \left[c_L \tfrac{1-\gamma^5}{2} + c_R \tfrac{1+\gamma^5}{2} \right] \ell Z^\mu, \tag{1.28}$$

  where $c_L = -1/2 + \sin^2\theta_W$, $c_R = \sin^2\theta_W$ and ℓ spans all six leptonic flavours[5].

[4] We remind: $\psi = \psi_L \psi_R + \psi_R \psi_L$.

[5] Recall $(1+\gamma^5)\nu = \nu_R = 0$.

We can now stop and highlight that: every leptonic current present in (1.26)-(1.28) can be written as:

$$J = \bar{\boldsymbol{\ell}}' C \mathbb{1} \boldsymbol{\ell}, \tag{1.29}$$

where ℓ and ℓ' are vectors containing initial and final flavour eigenstates, C is a constant operator and $\mathbb{1}$ the unit matrix. we have thus recovered the notion of *flavour universality* given above for all EW interactions of leptons, within the SM. We finally notice that for CC: $\boldsymbol{\ell}' \neq \boldsymbol{\ell}$; it means that initial and final flavour spaces are different: CC are so *flavour changing*.

Massive leptons. However, for leptons, no mass term has appeared yet. In the SM, indeed, leptons acquire mass as a result of the so called *Yukawa Mechanism*. It arises from the term of the total lagrangian:

$$\mathcal{L}^{l}_{Yuk} = \sum_{f=1}^{3} -\lambda^{f}(\bar{L^{f}_{L}}\phi E^{f}_{R} + \bar{E}^{f}_{R}\phi^{+}L^{f}_{L}). \tag{1.30}$$

Taking into account only the first family and imposing SSB, we get:

$$\mathcal{L}^{e}_{Yuk} = -\frac{\lambda^{e} v}{\sqrt{2}}(\bar{e}_{L}e_{R} + \bar{e}_{R}e_{L}) - \frac{\lambda^{e} H}{\sqrt{2}}(\bar{e}_{L}e_{R} + \bar{e}_{R}e_{L}). \tag{1.31}$$

Lagrangian (1.31), apart from establishing the coupling between the electron and the Higgs boson, permits to state: $m_e = \lambda^e v/\sqrt{2}$ and $m_{\nu_e} = 0$. We have so introduced the constant λ^e, called *Yukawa coupling* of the electron. The same can be done for the other families.

The point now is that: nothing but experiments can say if λ_e, λ_μ and λ_τ are equal or not. In the first case yukawa interactions for leptons are universal, in the second only *diagonal*[6]. Clearly nature chose the second case: $m_\tau : m_\mu : m_e \approx 4000 : 200 : 1$ [7]. SM does not explain why.

Quarks

The characterization of the EW scheme for quarks must allow for:

- 6 massive and charged flavour fields;
- both chiralities for each flavour;
- in CC: favourite transitions within families and suppressed (but observed) transition between families;

[6] We notice that a matrix is diagonal in one base may not be in another; only $\mathbb{1}$ has this property.

By virtue of that, GWS model formulates the following arrangement of multiplets:

QUARKS								
doublets	$\begin{pmatrix} u_L \\ d_L \end{pmatrix}$		$\begin{pmatrix} c_L \\ s_L \end{pmatrix}$		$\begin{pmatrix} t_L \\ b_L \end{pmatrix}$		Q_L^i	
singlets	u_R	d_R	c_R	s_R	t_R	b_R	U_R^i	D_R^i

Quantum numbers list is one more time presented in Table 1.1. Again $i = 1, 2, 3$ is related to the family.

Since all quark fields are massive, the Yukawa lagrangian is slightly more complex [16, §22.5.2]:

$$\mathcal{L}^q_{Yuk} = -\sqrt{2} \sum_{i,j=1}^{3} \left[\bar{Q}^i_L \phi f^-_{ij} D^j_R + \bar{Q}^i_L \tilde{\phi} f^+_{ij} U^j_R + \ h.c. \right] \tag{1.32}$$

where $\tilde{\phi} = i\sigma_2 \phi^*$ is the Higgs charge conjugated doublet, and the constant coefficients $f^{\pm}_{ij}$ form in general two matrices ($\mathsf{F}^{\pm}$) of couplings. Applying Brout-Englert-Higgs mechanism (SSB) and omitting the terms of interaction with the Higgs boson, the Yukawa lagrangian for quarks becomes:

$$\mathcal{L}^q_{Yuk} \supset -\begin{pmatrix} \bar{u}_L & \bar{c}_L & \bar{t}_L \end{pmatrix} (v\mathsf{F}^+) \begin{pmatrix} u_R \\ c_R \\ t_R \end{pmatrix} - \begin{pmatrix} \bar{d}_L & \bar{s}_L & \bar{b}_L \end{pmatrix} (v\mathsf{F}^-) \begin{pmatrix} d_R \\ s_R \\ b_R \end{pmatrix} \tag{1.33}$$

$$\mathcal{L}^{quark}_{Yuk} \supset -\left[\bar{\boldsymbol{q}}_{L+} \tilde{\mathsf{F}}^+ \boldsymbol{q}_{R+} + \bar{\boldsymbol{q}}'_{L-} \tilde{\mathsf{F}}^- \boldsymbol{q}'_{R-} \right] \tag{1.34}$$

with an evident notation introduced by the (1.34). It can be shown [28, 29] that $\tilde{\mathsf{F}}^{\pm}$ can both be made Hermitian, γ^5-free, and, above all, *diagonal* by making four separate unitary transformation on the "generation triplets". Explicitly:

$$(1.34) = -\left[\underbrace{\bar{\boldsymbol{q}}_{L+} V_+}_{\bar{\boldsymbol{q}}^{\circledast}_{L+}} \overbrace{V_+^\dagger \tilde{\mathsf{F}}^+ U_+}^{\mathsf{M}^+} \underbrace{U_+^\dagger \boldsymbol{q}_{R+}}_{\boldsymbol{q}^{\circledast}_{R+}} + \overbrace{\bar{\boldsymbol{q}}_{L-} V_-}^{\bar{\boldsymbol{q}}^{\circledast}_{L-}} \underbrace{V_-^\dagger \tilde{\mathsf{F}}^- U_-}_{\mathsf{M}^-} \overbrace{U_-^\dagger \boldsymbol{q}_{R-}}^{\boldsymbol{q}^{\circledast}_{R-}} \right] \tag{1.35}$$

$$= m_u \bar{u}^{\circledast} u^{\circledast} + m_c \bar{c}^{\circledast} c^{\circledast} + m_t \bar{t}^{\circledast} t^{\circledast} + m_d \bar{d}^{\circledast} d^{\circledast} + m_s \bar{s}^{\circledast} s^{\circledast} + m_b \bar{b}^{\circledast} b^{\circledast} \tag{1.36}$$

where as requested $\mathsf{M}^+ = \mathrm{diag}(m_u,\ m_c,\ m_t)$, $\mathsf{M}^- = \mathrm{diag}(m_d,\ m_s,\ m_b)$; the superscript $\circledast$ has been introduced to flag the appeared eigenstates of mass. Once again, SM is totally powerless in explaining differences between quark masses [7], which are de facto external inputs for this theory. Ergo, Yukawa interaction is diagonal for quark flavours too. Better, it is diagonal if we refer flavour to mass eigenstates.

What has just been shown for the Yukawa mechanism, has paramount effects on the observed electroweak phenomenology of the quarks. By complete analogy with the leptonic case, the following lagrangian of interaction can be assumed:

$$\mathcal{L}^q_{INT} = \sum_{i=1}^{3} g J^{i\mu}_j b^j_\mu + g' J^{i\mu}_Y \mathcal{A}_\mu. \tag{1.37}$$

The Noether's currents for the global symmetries $SU(2)_L$ and $U(1)_Y$ are respectively:

$$J^{i\mu}_j = \bar{Q}^i_L \gamma^\mu \frac{\sigma_j}{2} Q^i_L; \tag{1.38}$$

$$J^{i\mu}_Y = \tfrac{1}{3}\bar{Q}^i_L \gamma^\mu Q^i_L + \tfrac{4}{3}\bar{U}^i_R \gamma^\mu U^i_{R+} - \tfrac{2}{3}\bar{D}^i_R \gamma^\mu D^i_R. \tag{1.39}$$

As in the leptonic case $\mathcal{L}^{INT}_q = \mathcal{L}^{CC}_q + \mathcal{L}^{Neut.}_q$, with:

$$\mathcal{L}^{CC}_q = \sum_i g(J^{i\mu}_1 b^1_\mu + J^{i\mu}_2 b^2_\mu) = \sum_i \frac{g}{\sqrt{2}}[J^{i\mu}_+ W^-_\mu + J^{i\mu}_- W^+_\mu], \tag{1.40}$$

which this time explicitly is:

$$\mathcal{L}^{CC}_q = \frac{g}{\sqrt{2}}[\bar{\boldsymbol{q}}_{L-} \gamma^\mu \boldsymbol{q}_{L+} W^-_\mu + h.c.]. \tag{1.41}$$

Physical eigenstates can now be introduced in this way:

$$\mathcal{L}^{CC}_q = \frac{g}{\sqrt{2}}[\bar{\boldsymbol{q}}^{\circledast}_{L-} V^\dagger_- V_+ \boldsymbol{q}^{\circledast}_{L+} \gamma^\mu W^-_\mu + h.c.]. \tag{1.42}$$

The crucial matrix $V^\dagger_- V_+ \equiv V_{CKM}$ is called CKM matrix after Cabibbo-Kobayashi-Maskawa [6, 30]. It can be demonstrated that V_{CKM} is unitary, while there are no reasons which imply it to be diagonal. As a result, SM can incorporate the observed charged transitions between quarks belonging to distinct families.

We shall now commit an abuse of notation, dropping superscripts $\circledast$, but *still referring to mass eigenstates*. After that, the CC lagrangian can be written as:

$$\mathcal{L}^{CC}_q = \frac{g}{\sqrt{2}} \begin{pmatrix} \bar{u}_L & \bar{c}_L & \bar{t}_L \end{pmatrix} \begin{pmatrix} V_{ud} & V_{us} & V_{ub} \\ V_{cd} & V_{cs} & V_{cb} \\ V_{td} & V_{ts} & V_{tb} \end{pmatrix} \gamma^\mu \begin{pmatrix} d_L \\ s_L \\ b_L \end{pmatrix} W^+_\mu + h.c. \tag{1.43}$$

which plainly manifests elements of V_{CKM} as coupling constants between up-like and down-like mass eigenstates of quarks. As a result weak charged interaction is not flavour universal about mass eigenstates.

Nonetheless, a small step brings to a meaningful point of view:

$$\mathcal{L}^{CC}_q = \frac{g}{\sqrt{2}}[(\bar{u}_L \gamma^\mu d'^\mu_L + \bar{c}_L \gamma^\mu s'^\mu_L + \bar{t}_L \gamma^\mu b'^\mu_L) W^+_\mu + h.c.] \tag{1.44}$$

with:

$$\begin{pmatrix} d'_L \\ s'_L \\ b'_L \end{pmatrix} = \begin{pmatrix} V_{ud} & V_{us} & V_{ub} \\ V_{cd} & V_{cs} & V_{cb} \\ V_{td} & V_{ts} & V_{tb} \end{pmatrix} \begin{pmatrix} d_L \\ s_L \\ b_L \end{pmatrix}. \tag{1.45}$$

In this scheme V_{CKM} rules the **mixing** between the mass eigenstates and the, so called, "weak eigenstates". The interaction lagrangian (1.44) is equal to the leptonic one (1.26) and we can say that, in this representation, charged weak interaction is flavour universal also for quarks.

1.3 CKM matrix

As said, SM requires V_{CKM} to be unitary. Besides it can be demonstrated that V_{CKM} is completely defined by only four parameters: three real, one complex phase. Real parameters can be thought as rotation angles in a 3D flavour space. With reference to Fig. 1.2, we define: θ_{12} as the angle around b axis, θ_{13} around s axis and θ_{23} around d axis. To speed up the notation we are going to use: $c_{ij} = \cos\theta_{ij}$ and $s_{ij} = \sin\theta_{ij}$. The real part of the CKM matrix can be written as:

$$V_{real} = \begin{pmatrix} 1 & 0 & 0 \\ 0 & c_{23} & s_{23} \\ 0 & -s_{23} & c_{23} \end{pmatrix} \begin{pmatrix} c_{13} & 0 & s_{13} \\ 0 & 1 & 0 \\ -s_{13} & 0 & c_{13} \end{pmatrix} \begin{pmatrix} c_{12} & -s_{12} & 0 \\ s_{12} & c_{12} & 0 \\ 0 & 0 & 1 \end{pmatrix} \tag{1.46}$$

The complex phase can be introduced in this way:

$$\begin{aligned} V &= \begin{pmatrix} 1 & 0 & 0 \\ 0 & c_{23} & s_{23} \\ 0 & -s_{23} & c_{23} \end{pmatrix} \begin{pmatrix} c_{13} & 0 & s_{13}e^{-i\delta_{13}} \\ 0 & 1 & s0 \\ -s_{13}e^{+i\delta_{13}} & 0 & c_{13} \end{pmatrix} \begin{pmatrix} c_{12} & -s_{12} & 0 \\ s_{12} & c_{12} & 0 \\ 0 & 0 & 1 \end{pmatrix} \\ &= \begin{pmatrix} c_{12}c_{13} & s_{12}c_{13} & s_{13}e^{-i\delta_{13}} \\ -s_{12}c_{23} - c_{12}s_{23}s_{13}e^{+i\delta_{13}} & c_{12}c_{23} - s_{12}s_{23}s_{13}e^{+i\delta_{13}} & s_{23}c_{13} \\ s_{12}s_{23} - c_{12}c_{23}s_{13}e^{+i\delta_{13}} & -c_{12}s_{23} - s_{12}c_{23}s_{13}e^{+i\delta_{13}} & c_{23}c_{13} \end{pmatrix} \end{aligned} \tag{1.47}$$

One can observe that (1.47) is allowed because of the unitary nature of V_{CKM}. This latter condition can be experimentally checked, measuring the values of flavour parameters which compose the matrix. The results currently accepted are [7]:

$$\theta_{12} = (13.0005 \pm 0.0005)^\circ, \quad \theta_{23} = (2.387 \pm 0.013)^\circ, \quad \theta_{13} = (0.202 \pm 0.006)^\circ, \quad \delta_{13} = (68 \pm 3)^\circ \tag{1.48}$$

and the CKM matrix becomes [7]:

$$V = \begin{pmatrix} 974.34^{+0.11}_{-0.12} & 225.06 \pm 0.50 & 3.57 \pm 0.15 \\ 224.92 \pm 0.5 & 973.51 \pm 0.13 & 41.1 \pm 1.3 \\ 8.75^{+0.32}_{-0.33} & 40.3 \pm 1.3 & 999.15 \pm 0.05 \end{pmatrix} \times 10^{-3}. \tag{1.49}$$

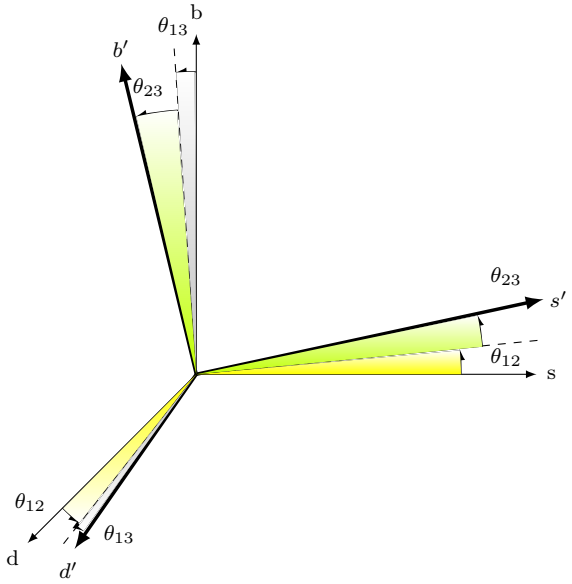

Figure 1.2: Quark rotation

Squared modules of V_{CKM} elements are, in fact, transitions rates from *up-like* states to *down-like* ones, or vice versa. On the grounds of that a first test of the theoretical hypothesises is possible: the sum of the squared module along row and column must be one. The experimental results are [7]:

$$
\begin{aligned}
|V_{ud}|^2 + |V_{us}|^2 + |V_{ub}|^2 &= 0.9996 \pm 0.0005 \qquad 1^{st}\ row \\
|V_{cd}|^2 + |V_{cs}|^2 + |V_{cb}|^2 &= 1.040 \pm 0.0032 \qquad 2^{nd}\ row \\
|V_{tc}|^2 + |V_{ts}|^2 + |V_{tb}|^2 &= 1.02 \pm 0.06 \qquad 3^{rd}\ row \\
|V_{ud}|^2 + |V_{cd}|^2 + |V_{td}|^2 &= 0.9975 \pm 0.0022 \qquad 1^{st}\ col. \\
|V_{us}|^2 + |V_{cs}|^2 + |V_{ts}|^2 &= 1.042 \pm 0.0032 \qquad 2^{nd}\ col. \\
|V_{ub}|^2 + |V_{cb}|^2 + |V_{tb}|^2 &= 1.02 \pm 0.06 \qquad 3^{rd}\ col.
\end{aligned}
$$

By observation of the elements of the CKM matrix reported in (1.49), a clear hierarchy can be found. As graphically displayed by Fig. 1.3 diagonal terms are close to 1, meaning that transition within the families are favoured. Besides, the mixing between the first and the second family is bigger than the mixing between the first one and the third one, which is strongly suppressed.

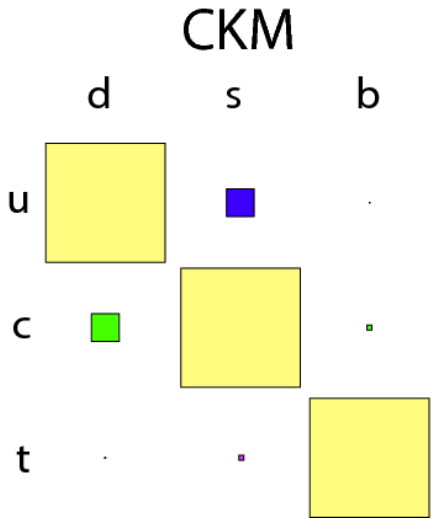

Figure 1.3: Graphical representation of the relative magnitude of V_{CKM} elements.

Chapter 2

Test of LFUV: $\mathcal{R}_{D^*}$

2.1 Standard Model Prediction

Following [5, 31, 32], the relevant effective Hamiltonian for the semileptonic transition $b \to c\ell\bar{\nu}_\ell$ is:

$$H_{eff} = \frac{4G_F V_{cb}}{\sqrt{2}} J_{bc,\mu} \sum_{\ell=e,\mu,\tau} (\bar{\ell}\gamma^\mu P_L \nu_\ell) + h.c., \tag{2.1}$$

where J^μ_{bc} is the charged current for $b \to c$, according to the SM:

$$J^\mu_{bc} = \bar{c}\gamma^\mu P_L b, \tag{2.2}$$

with $P_L = (1-\gamma^5)/2$. Starting from (2.1), the transition rate for the process $\bar{B}^0 \to D^{*+}\ell^-\bar{\nu}_\ell$ can be calculated as a function of the transferred 4-momentum $q^2 = (p^\mu_B - p^\mu_{D^*})^2$:

$$\frac{d\Gamma_\ell}{dq^2} = \frac{G_F^2 |V_{cb}|^2 |\boldsymbol{p}| q^2}{96\pi^3 m_B^2} \left(1 - \frac{m_\ell^2}{q^2}\right)^2 \left[\left(|H_{++}|^2 + |H_{--}|^2 + |H_{00}|^2\right) \left(1 + \frac{m_\ell^2}{2q^2}\right) + \frac{3}{2}\frac{m_\ell^2}{q^2} |H_{0s}|^2 \right] \tag{2.3}$$

where $|\boldsymbol{p}| = \frac{\sqrt{\lambda(m_B^2, m_{D^*}^2, q^2)}}{2m_B}$, with $\lambda(a,b,c) = a^2 + b^2 + c^2 - 2(ab + ac + bc)$, is the module of the 3-momentum of the D^* meson in the B^0 rest frame. Terms H_{mn} represent the helicity amplitudes for transitions from the initial state, whose helicity is fixed, to the final states whose helicities are reported in the subscripts:

$$\begin{aligned}
H_{\pm\pm}(q^2) &= (m_B + m_{D^*}) A_1(q^2) \mp \frac{2m_B |\boldsymbol{p}|}{m_B + m_{D^*}} V(q^2), \\
H_{00}(q^2) &= \frac{1}{2m_{D^*}\sqrt{q^2}} \left[(m_B^2 - m_{D^*}^2 - q^2)(m_B + m_{D^*}) A_1(q^2) - \frac{4m_B^2 |\boldsymbol{p}|^2}{m_B + m_{D^*}} A_2(q^2) \right], \\
H_{0s}(q^2) &= \frac{2m_B |\boldsymbol{p}|}{\sqrt{q^2}} A_0(q^2);
\end{aligned} \tag{2.4}$$

where $A_0(q^2)$, $A_1(q^2)$, $A_2(q^2)$ and $V(q^2)$ are form factors (FF), which describe the non-perturbative hadronic interactions in $B^0 \to D^{*-}\tau^+\nu_\tau$. One possible parametrization [1] exploits the scalar product of the B and D^* four-velocities:

$$w = v_B \cdot v_{D^*} = \frac{m_B^2 - m_{D^*}^2 - q^2}{2m_B m_{D^*}}, \tag{2.5}$$

After that, it is convenient to express FF in terms of a universal FF $h_{A_1}(w)$ and ratios $R_i(w)$:

$$\begin{aligned} A_1(w) =& \frac{(w+1)\tilde{r}}{2} h_{A_1}(w); \quad A_0(w) = \frac{R_0(w)}{\tilde{r}} h_{A_1}(w); \\ A_2(w) =& \frac{R_2(w)}{\tilde{r}} h_{A_1}(w); \quad V(w) = \frac{R_1(w)}{\tilde{r}} h_{A_1}(w); \end{aligned} \tag{2.6}$$

with $\tilde{r} = \frac{\sqrt{2m_B m_{D^*}}}{m_B + m_{D^*}}$. Using dispersion relations and analyticity constraints [5, 33], the universal FF and the ratios can be expressed in term of just five parameters:

$$\begin{aligned} h_{A_1}(w) =& h_{A_1}(1)[1 - 8\rho_{D^*}^2 z(w) + (53\rho_{D^*}^2 - 15)z^2(w) - (231\rho_{D^*}^2 - 91)z^3(w)]; \\ R_1(w) =& R_1(1) - 0.12(w-1) + 0.05(w-1)^2; \\ R_2(w) =& R_2(1) + 0.11(w-1) - 0.06(w-1)^2; \\ R_0(w) =& R_0(1) - 0.11(w-1) + 0.01(w-1)^2. \end{aligned} \tag{2.7}$$

Here, $z(w) = (\sqrt{w+1} - \sqrt{2})/(\sqrt{w+1} + \sqrt{2})$. Instead, the FF parameters $R_1(w)$, $R_2(w)$ and $\rho_{D^*}^2$ are measurable in analysis of $B \to \ell\tau^+\nu_\ell$ decays. According to Heavy Flavour Averaging Group (HFAG) [4] their values are:

$$R_1(w) = 1.401 \pm 0.033; \quad R_2(w) = 0.854 \pm 0.020; \quad \rho_{D^*}^2 = 1.207 \pm 0.028. \tag{2.8}$$

$R_0(w)$ affects the dacay rate only via the scalar hadronic amplitude $H_{0s}(q^2)$. The corresponding leptonic amplitude is helicity suppressed, *i.e.*, its rate is proportional to the mass of the mass of the lepton. As a result, $B \to \ell\tau^+\nu_\ell$ decays are not sensitive to this FF, and $R_0(w)$ has not been measured. Its theoretical estimation is $R_0(1) = 1.14 \pm 0.07$, based on HQET [5].

Because of the differences of mass among leptons, the last term of (2.3) is important only if $\ell = \tau$. On the contrary, the phase space term $(1 - m_l^2/q^2)^2$ suppresses channels with τ with respect to the others.

Uncertainties due to the form factors for the hadronic transitions can be reduced taking into account the ratio between the the case with $\ell = \tau$ and $\ell = e, \mu$. By virtue of that a worthy observable is:

$$\mathcal{R}_{D^*} = \frac{\mathcal{B}(\bar{B}^0 \to D^{*+}\tau^-\bar{\nu}_\tau)}{\mathcal{B}(\bar{B}^0 \to D^{*+}\mu^-\bar{\nu}_\mu)} \tag{2.9}$$

We can notice, in fact, that the factor $h_{A_1}(1)$ only affect the overall normalization, then it cancels in $\mathcal{R}_{D^*}$. Explicitly we have:

$$\mathcal{R}_{D^*}(q^2) = \frac{d\Gamma_\tau/dq^2}{d\Gamma_{e,\mu}/dq^2} = \left(1 - \frac{m_\tau^2}{q^2}\right)^2 \left[\left(1 + \frac{m_\tau^2}{2q^2}\right) + \frac{3m_\tau^2}{2q^2} \frac{|H_{0s}|^2}{(|H_{++}|^2 + |H_{--}|^2 + |H_{00}|^2)}\right] \tag{2.10}$$

This expression suggests that also the correlation among FFs may be reduced in the ratio. Integrating (2.10) on q^2, we finally get the SM prediction:

$$\boxed{\mathcal{R}_{D^*}^{SM} = 0.252 \pm 0.003}. \tag{2.11}$$

The given uncertainty is mainly dominated by the estimation of higher order perturbative terms and by "heavy quark approximation" [34].

2.2 New Physics in $b \to c\ell\bar{\nu}_\ell$

The presence of a τ lepton can enhance new physics (NP) contributions which remain suppressed when lighter leptons appear [31]. Such phenomena can be describe by effective theories by writing J_{bc}^μ as a total derivative of a scalar operator. As a consequence, the study shown in [5] modifies (2.1) choosing to let intact the $V-A$ structure of the leptonic part. Specifically, the hadronic current is expanded in:

$$J_{bc}^\mu = \bar{c}\gamma^\mu P_L b + g_{SL} i\partial^\mu(\bar{c}P_L b) + g_{SR} i\partial^\mu(\bar{c}P_R b) \tag{2.12}$$

where the first term comes from SM, while g_{SL} and g_{SR} are dimensionful couplings due to NP. If NP come at a scale big enough ($\Lambda_{NP} \gg v$, where v is the vacuum expectation value of EW theory) then we expect: $g_{SL,SR} \sim 1/\Lambda_{NP}$. Besides it can be shown that NP charged current as (2.12) only affect H_{0s}, which can be written as:

$$H_{0s} = H_{0s}^{SM}\left[1 + (g_{SR} - g_{SL})\frac{q^2}{m_b + m_c}\right]. \tag{2.13}$$

It is now possible to evaluate the impact of NP on R_{D^*}:

$$\mathcal{R}_{D^*} = R_{D^*}^{SM}\left\{1 + 0.12\mathrm{Re}\left[m_\tau(g_{SR} - g_{SL})\right] + 0.05|m_\tau(g_{SR} - g_{SL})|^2\right\} \tag{2.14}$$

The experimental measurement of $\mathcal{R}_{D^*}$ allow then to constrain the difference between the new couplings: $g_{SR} - g_{SL}$. Merging this to other results[1] should be possible to estimate a energetic scale for NP.

Several theories Beyond the Standard Model (BSM) predict modification to $\mathcal{R}_{D^*}$. Among them we remember: models with two charged doublet of higgs bosons (2HDM) of II or III kind, the leptoquark model, and the existence of new, tensorial or scalar, mediators provided of colour charge.

[1] For example the measurement of $R_D \equiv \frac{BR(\bar{B}^0 \to D^+ \tau^- \bar{\nu}_\tau)}{BR(\bar{B}^0 \to D^+ \mu^- \bar{\nu}_\mu)}$ should depend on $g_{SR} + g_{SL}$ [5].

Chapter 3

The LHCb detector at LHC1

3.1 The Large Hadron Collider

The Large Hadron Collider (LHC [35]) is the largest particle accelerator in the world. It is located at CERN laboratories, near Geneva, in the 100 m underground tunnel that previously hosted LEP accelerator. The main characteristics of this machine are resumed in Tab. 3.1.
The main experiments now in operation at the LHC are:

- ALICE: designed to study the hadronic state called "quark-gluon plasma", produced by collisions between heavy nuclei (*e.g.* Pb-Pb).
- ATLAS and CMS: multi purpose-detectors, designed for direct search of new physics (NP). In 2012 they obtained the first direct observation of the Higgs boson.
- LHCb: designed to study CP violation. The LHCb experiment searches for indirect evidences of NP in the charm and beauty quarks sectors, and also specifically oriented to indirect search for NP.

3.2 The LHCb detector

The first feature of LHCb experiment is the high statistic it can collect. This is due to the large production cross section for beauty quarks pairs, $\sigma_{b\bar{b}} = (283 \pm 53)\ \mu$b, and charm quarks pairs, $\sigma_{c\bar{c}} = (6.1 \pm 0.93)$ mb in high energy pp collisions [7]. The high luminosity condition results in an enhanced probability of pile-up events. They represent on of the main problems for the LHCb experiment, since a reconstruction of decay chains with main interaction vertices, together with good particle identification (PID) performances is needed. For these reasons, an appropriate beam focusing system reduces the instantaneous luminosity at LHCb interaction site (see Tab. 3.1).

Run	**1**
Years	2011-12
$\sqrt{s}$	8
Circumference	26.7 Km
Max instantaneous luminosity	$10^{34}\ cm^{-2}s^{-1}$
LHCb instantaneous luminosity	$2 \times 10^{32}\ cm^{-2}s^{-1}$
LHCb integrated luminosity	3 fb^{-1}
Bunch crossing frequency	40 MHz
$p-p$ cross section	100 mb
B_{dipols}	~ 8 T
Protons per bunch	$\sim 10^{11}$

Table 3.1: LHC essential parameters.

Due to the imbalance in momentum of two partons that collied during a pp interaction, the $b\bar{b}$ and $c\bar{c}$ pairs are produced in the same forward (or backward) direction. As a consequence, the LHCb experiment is designed as a single-arm forward spectometer. Its geometrical acceptance covers the pseudorapidity[1] range $2 < \eta < 5$ in the bending plane, which corresponds to $0°36' < \theta < 17°$, if θ names the elevation angle from the beam direction (yz plane)[2].

The LHCb detector total length is about 20 meters. According to the forward spectometer configuration several subdetectors are disposed one after the other along the beam pipe direction. The general scheme is illustrated in Fig. 3.1. The LHCb subdetectors can be divided in two differen categories.

- The tracking systems: Vertex Locator (VELO), Tracker Turicensis (TT) and the three tracking stations (T1-T3). The aim of the tracking systems is to reconstruct the tracks from the hits in the various apparatus and to measure particle momenta through their curvature in a magnetic field.

- The PID systems: two Ring Imaging Cherenkov detectors (RICH1 and RICH2), the calorimeter system (PS, SPD, ECAL and HCAL) and five muon stations (M1-M5). The goal of the PID systems is to identify particles that cross the detector exploiting theri different behaviour when interacting with different materials.

In the following , a more detailed description of the various sub-detectors will be given.

[1] $\eta = -\log(\tan\theta/2)$.

[2] In the xz plane the acceptance is slightly smaller: $0°36' < \theta < 14°$, where θ is the azimuthal angle.

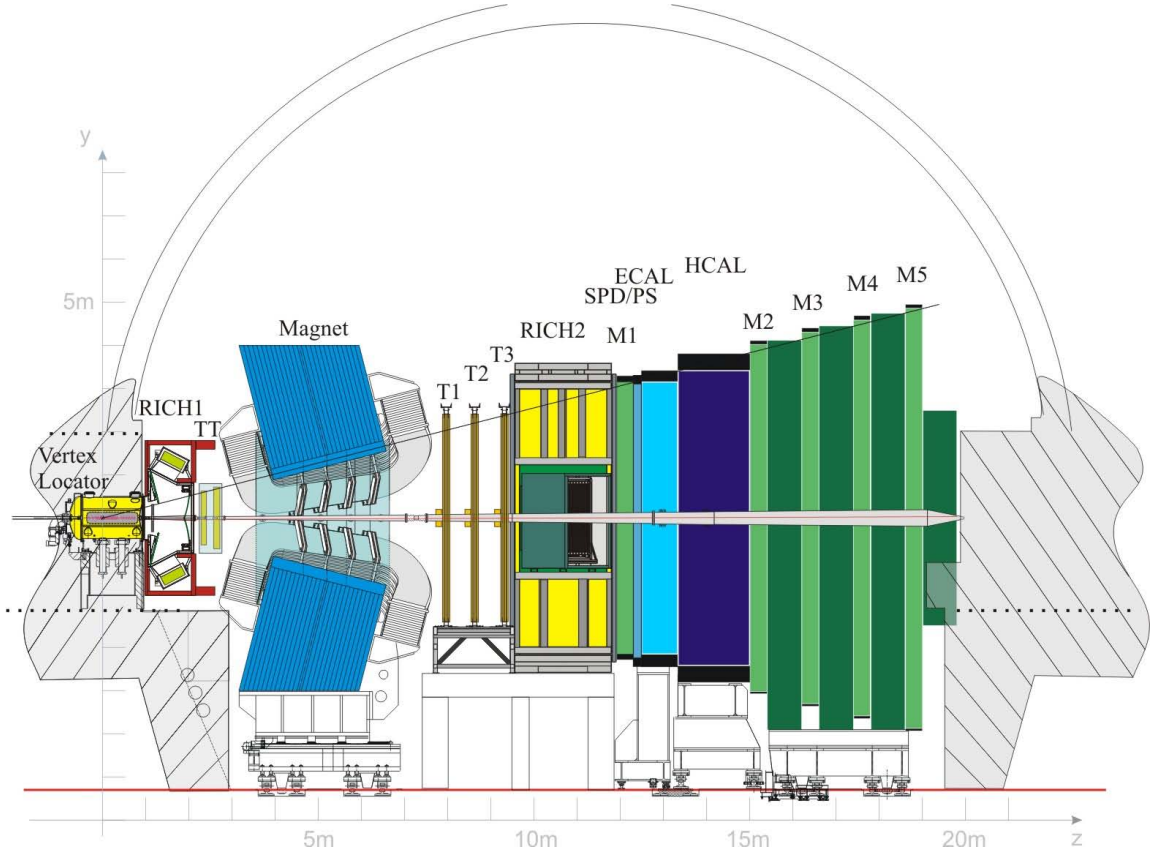

Figure 3.1: LHCb general scheme.

3.2.1 Tracking System

The tracking system is composed by the Vertex Locator placed around the collision point, and Trigger-Tracking planes situated before (TT) and after (T1-T3) the dipole magnet. The VELO and TT are completely made of silicon micro-strips. This technology also used in the T1-T3 regions closer to the beam pipe; commonly referred to as Inner Tracker (IT). The outer sectors of T1-T3, called Outer Tracker (OT) are made instead of straw-tubes. The combination of TT and IT is usually named "Silicon Tracker".

VELO. The LHC proton beams run across the entire length of the detector protected by a beryllium pipe. The VELO is located at the point where the beams collide. Its task consists in identifying the primary and secondary vertices. In fact, B and D mesons have average lifetimes of $\sim 10^{-12}$ s and travel a distance of about 1 cm before decaying. This sub-detector is made up of a series of crescent-shaped silicon modules, perpendicular to the direction of the beam. Each module is 0.3 mm thick and consists of two types of

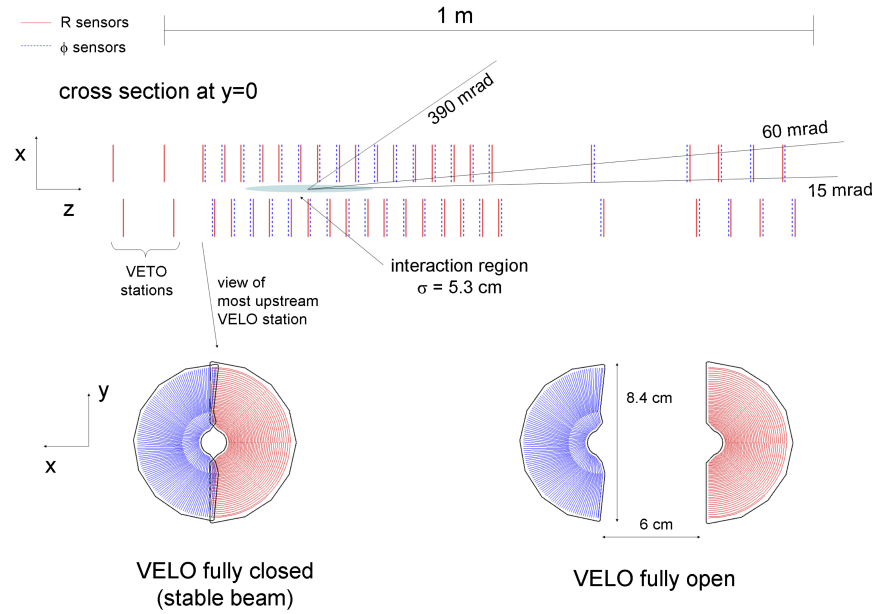

Figure 3.2: (top) Top view of the VELO and (bottom) frontal view of the VELO in (left) open and (right) closed position, respectively. The R sensors are represented in red while the ϕ sensors are drawn in blue.

sensors named R and ϕ. The former are segmented into concentric silicon strips, whereas the latter sensors are radially segmented. The R sensors measure radial position, while ϕ sensors measure the azimuthal coordinate. Each sensor has an amplitude of 182° (Fig. 3.2). To improve the measurement of the primary vertex, the VELO, in addition to covering the entire angular acceptance forward, also partially covers the backward hemisphere.

Fig. 3.2 also displays the two possible VELO arrangements: *Fully Closed* and *Fully Open*. The first one is the working configuration, the second one, instead, is exploited during beam stabilization phase or during maintenance.

Trigger Tracker. The TT is positioned after the first RICH and before the entrance to the magnet. Its inner part (IT) is composed by silicon micro-strip sensors with a $\sim 200\mu$m step. Their efficiency exceeds 99.8%. The main purpose of this sub-detector to provide information to the first level of trigger to estimate the momentum of tracks with high impact parameter.
The Trigger Tracker is made up of 4 layers. The first and fourth have vertical reading strips and measure the bending coordinate x, the second and third, instead, measure the

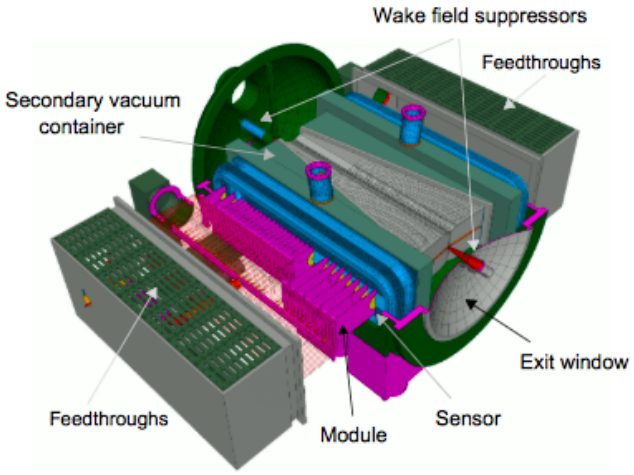

Figure 3.3: VELO three-dimensional structure.

z coordinate thanks to strips rotated of $+5°$ and $-5°$, with respect to the previous ones. The TT dimensions are 150×130 cm^2 and thus it covers the entire detector acceptance.

Tracking Stations. The *Inner Tracker* (IT) is the inner part of the Tracking Stations. It is located after the magnet and it is divided into three equidistant stations (T1, T2, T3), positioned at the coordinate $z = 7.67,\ 8.36,\ 9.05$ m. Each station is divided into 4 layers of detectors. The first two layers have vertical cells, while the second and third are composed of circular cells, offset by a stereo angle of $\pm 5°$. This arrangement ensures a precise measurement of the pulse and sufficient resolution for the reconstruction of the traces in the vertical plane. The *Inner Tracker* has a surface of about 120×40 cm^2, in the shape of a cross around the beam pipe (see Fig. 3.4).

The shape of the *Silicon Tracker* is the result of the following considerations.

- **Spatial resolution.** For both TT and IT, a single hit resolution of 50 μm is required to have a fairly accurate pulse measurement.
- **Hit occupancy.** The flow of particles in the Inner Tracker is about 5×10^{-2} particles per cm^2. Instead in the outer region the flow is reduced by two orders of magnitude.
- **Signal formation.** The signal is formed in a time of the order of the collision frequency of LHC (25 ns) to avoid mainly the *pile-up* of events originating from consecutive collisions.

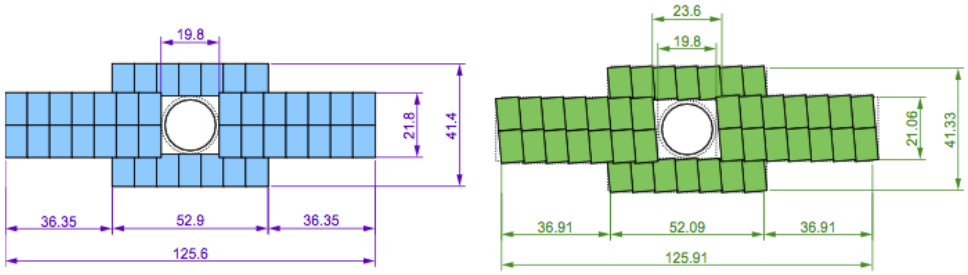

Figure 3.4: (left) first and (right) third planes composing the Inner Tracker. Both figures are relative to the xy plane. The reported dimensions are in cm.

- **Single hit efficiency.** For maximum efficiency on every single hit the signal to noise ratio S/N (*Signal-to-Noise*) must be greater than 10.

The *Outer Tracker* (OT) is essentially a drift detector and consists of 2 layers of 64 straw-tubes. Each straw tube has an inner diameter of 4.9 mm and walls 75 μm thick. It is filled with a gaseous mixture consisting of Argon (70%) and CO_2 (30%). In these conditions the drift time is less than the time interval between two collisions at LHC, (< 25 ns), and the resolution achieved 200 μm. Each module consists of 3 stations each with a total active area of 5971×4850 mm^2.

3.2.2 Particle identification systems

The particle identification system consists of two *Ring-Imaging Cherenkov* (RICH) detectors, two calorimeters and a muon detector. As shown in Fig. 3.1, the RICH1 is located just after the VELO, while the RICH2 is immediately after the last *Tracking Station*. Subsequently ECAL and HCAL are placed before the muon detector.

RICH. RICH detectors measure the emission of *Cherenkov* radiation. This arise when a charged particle travels through a medium, in this case gas, with a velocity higher than light in that medium. Through the analysis of the emitted radiation it is possible to distinguish with precision the protons, kaons and pions candidates. The RICH apparatus measures the *Cherenkov* angle θ_c through the formula:

$$\cos\theta_c = \frac{1}{n\frac{v}{c}}, \tag{3.1}$$

where v is the velocity of the particle, n is the refraction index of the medium and c is the light velocity in the vacuum. Fig. 3.5 displays the distribution of θ_c as a function of particle impulse. For given impulse different particles emit light with different *Cherenkov*

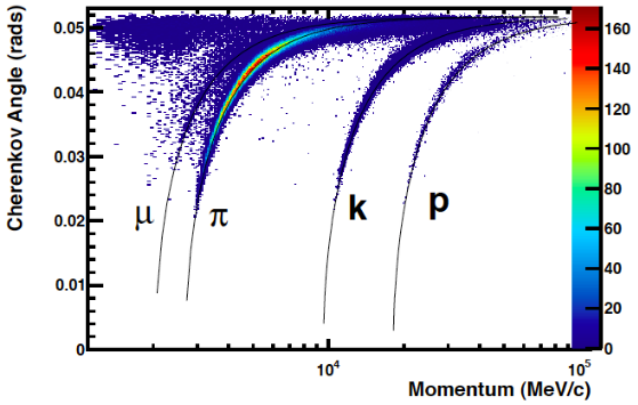

Figure 3.5: Cherenkov angle as function of momentum of particles.

angles.
In order to identify charged particles with momentum between 1 and 100 GeV/c two RICH detectors are needed. The RICH1 optimally identifies particles with a pulse between 10 and 60 GeV/c; RICH2 instead is accurate for particles with a pulse between 60 and 100 GeV/c. The RICH1 (Fig. 3.6) consists of two different radiator media: aerogel and fluorobutane (C_4F_{10}). Aerogel is a colloidal form of quartz, with an extremely low density, but with a refractive index in the range 1.01-1.10; these characteristics make it suitable for detecting particles with a low impulse (few GeV/c). Fluorobutane has a refractive index of 1.0014 and allows the identification of particles with a higher pulse. The RICH2 (Fig. 3.6) is composed of a single radiant medium: tetrafluoromethane (CF_4), which has a refractive index of 1,00048.
The photons produced by the particles travelling in the RICH detectors are conveyed, through a system composed by mirrors, onto a lattice of photo detectors, called Hybrid Photon Detector (HPD). To reduce possible deflections, ultra-light spherical mirrors, made of polymer-reinforced carbon fibers (CFRP), are used. Being placed after the tracking system, glass can be used to construct the spherical mirrors of RICH2. Both RICH utilize the HPD to measure the position of the emitted photons.

Calorimeters. Calorimeters are designed to measure the energy of the particles. Before ECAL two auxiliary detectors are installed: PS (*Preshower Detector*) and SPD (*Scintillator Pad Detector*). HCAL, instead, is installed immediately after ECAL. PS and SPD discriminate respectively the large background consisting of charged pions and charged particles from neutral ones. SPD, PS and ECAL are segmented into 3 zones

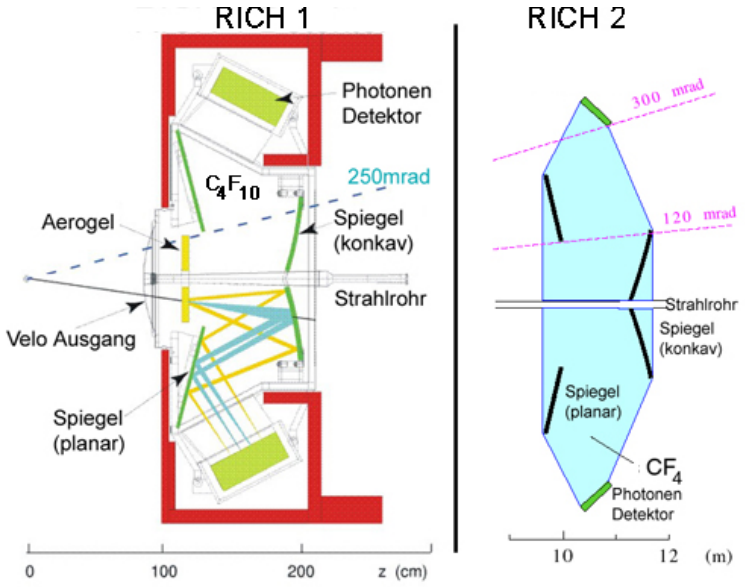

Figure 3.6: Scheme of RICH detectors.

composed of cells of different spatial area, as illustrated in Figure 3.7.

ECAL is composed of 2 mm thick sheets of lead interspersed by 4 mm thick scintillator plates. HCAL has a similar structure: 4 mm thick plastic scintillator plates alternating with 16 mm thick layers of iron. The scintillation light is transmitted to phototubes through WaveLenght-Shifting plastic fibers. The LHCb calorimeters can distinguish $e^{\pm}$ and $pi^{\pm}$ with a precision of 90% and a contamination of less than 1%.

Muon Detector. Muons are present in many decays of the B and D mesons, so the identification of muons is very important for the LHCb experiment. Located at the end of LHCb, the muon detection system consists of 5 rectangular Multi-Wire Proportional Chambers (MWPC) of increasing size (see Fig, 3.8). Each MWPC station contains cells filled with different gases: carbon dioxide, argon and methane tetrafluoride. There are a total of 1380 chambers and 2.5 million wires covering an area of about 435 m^2.

After the calorimeters system, the M2-M5 stations are interspersed with 80 cm thick iron absorbers. To be able to pass all the stations, a muon must have a threshold of about 6 GeV. The M1 station is the most important because it has to sustain a flow of particles higher than the others (about 250 kHz/cm^2) it is formed by two chambers *triple-GEM* (Gas Electron Multiplier) detectors overlapped.

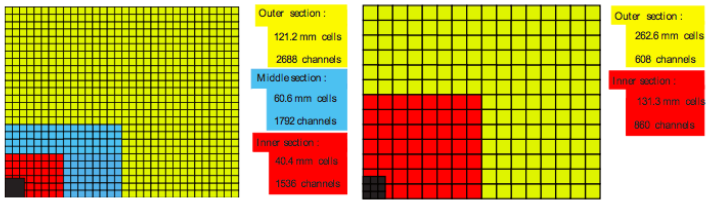

Figure 3.7: (left) PS, SPD and ECAL and (right) HCAL segmentation. Only a quarter of the total trasverse surface is shown.

The Magnet. The magnet, positioned between the TT and T1 detector (see Fig. 3.1), It consists of two coils, each 27 tons heavy of trapezoidal shape folded to 45° along the two transverse sides and mounted inside an armor of steel of 1450 tons (see Fig. 3.9); It is 4.3 meters long horizontally and 3.6 meters vertically. Each coil is made up of 10 layers covered by about 3000 meters of cables aluminum. The magnet is a warm dipole *i.e.* non superconducting. The maximum field intensity of the magnet is about 1T, while the integral of the magnetic field is approximately 4 Tm. During data acquisition, the polarity of the magnet is reversed several times to minimize the sysitematic effects due to left-right asymmetries of the detector.

3.2.3 The Trigger

The LHCb experiment works at an instantaneous luminosity of $2 \times 10^{32}\text{cm}^{-2}\text{s}^{-1}$, two orders of magnitude less than the nominal one of LHC. This characteristic has precise advantages: it facilitates the management of damage caused by radiation and it makes sure that there are only single collisions during the beam crossing, thus facilitating the reconstruction and the trigger itself. The collision frequency is of $\sim$ 40MHz and thanks to this data acquisition system is reduced to about 5 kHz. The Trigger System is composed of two levels: the Level-0 (L0) and the High Level Trigger (HLT). The former is implemented in the detection electronics, while the second is software that works on a CPU farm of thousands of nodes. The offline analysis rejects a large part of background events based on the masses of the B and D mesons, their average lifetimes and other stringent conditions.

L0. The objective of the Level-0 Trigger is to reduce the inflow of data from the frequency of bunch crossing of 40 MHz to 1 MHz. To do this, we some operations need to performed:

- identification of hadrons, electrons and photons with a transverse energy (E_{T})greater than a given threshold by analysing the information of the calorimeters systems;

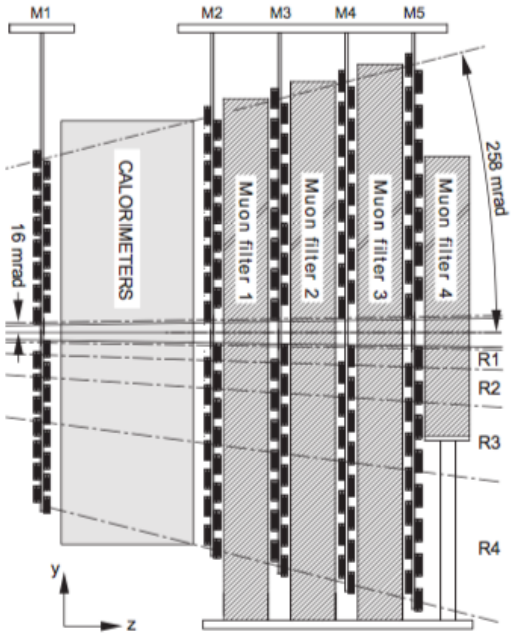

Figure 3.8: Lateral view of the 5 muon stations.

- reconstruction of muon pairs with the high transverse momentum;
- estimation of the total energy observed;
- calculation of the number of tracks based on the information on the hits obtained from the SPD.

HLT. The High Level Trigger is composed of two sub-levels: HLT1 and HLT2. The goal of HLT1 s to further reduce the rate obtained from the L0 output to a more manageable level. The request for tracks with high p_T and with a large impact parameter reduces the data rate to about 30 kHz. At this point the HLT2 refines the selection of the candidates, writing to the storage disks at a rate of 5kHz. The collected events are sent to the computing system present in CERN (Tier-0). Tier-0 will be responsible for distributing the data collected in the 6 Tier-1 calculation centers in Europe almost in real time. One of these six centers is based in Bologna (CNAF).

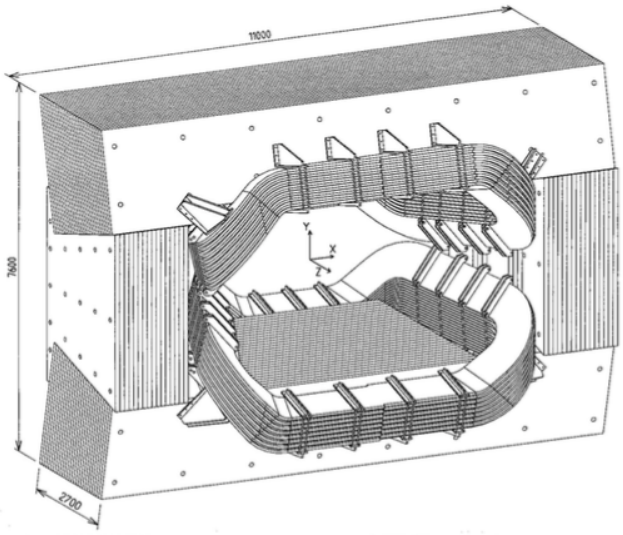

Figure 3.9: Section of the magnetic diopole.

Chapter 4

LHCb measurement of $\mathcal{R}_{D^*}$ 3-prong

This chapter describes the measurement of $\mathcal{R}_{D^*}$ performed by the LHCb Collaboration [13]. The focus is reserved to the estimation of $\mathcal{B}(B^0 \to D^{*-}\tau^+\nu_\tau)$[1], using as final state the τ^+ hadronic decay with three charged particles, $\tau^+ \to \pi^+\pi^-\pi^+(\pi^0)\bar{\nu_\tau}$, also called *3-prong*. The employed data sample was collected by the LHCb experiment during Run 1. The energy in the center of mass for the pp collisions was 7 TeV in 2011 and 8 TeV in 2012. The overall integrated luminosity collected was 3 fb^{-1}.

The analysis of this 3-prong mode is complementary to the measurement of $\mathcal{R}_{D^*}$ already performed by the LHCb collaboration, and based on τ^+ leptonic decays [3].

In particular the 3-prong configuration:

- avoids the difficult task of discriminating the τ^+-channel among the more abundant prompt semileptonic decays involving lighter leptons: $B^0 \to D^{*-}\tau^+(\to \ell^+\nu_\ell\bar{\nu}_\tau)\nu_\tau$ vs. $B^0 \to D^{*-}\ell^+\nu_\ell$, with $\ell = e, \mu$;
- allows to reconstruct the τ decay vertex. This gives a powerful criterium to discriminate between the signal and the most abundant background source due to prompt hadronic decays of the B^0 meson (§4.3);
- permits to close the kinematics of the τ^+ and B^0 dacays. Since a single neutrino is present in each of their decays, the knowledge of the direction of τ^+ and B^0 grants the estimation of all 4-momenta, up to a two fold ambiguity (§4.4).

Nevertheless, the signal extraction remains an onerous effort. To suppress at a very large extent the other background sources, novel partial reconstruction techniques and isolation tools (based on charged but also neutral particles) were developed by the LHCb Collaboration (§4.3.2). Another efficient tool to isolate the signal is the different 3π dynamics observed in τ^+ and D_s^+ decays; it led to the implementation of a multivariate analysis (`BDT`), whose output was exploited, on one hand to enhance signal purity, and on

[1] The inclusion of the charged-conjugated modes is always implied in this study.

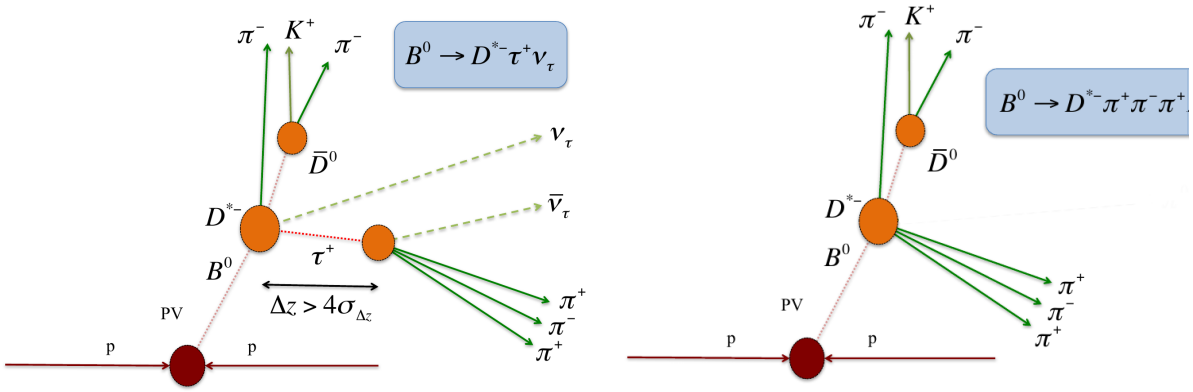

(a) *Signal* **(b)** *Normalization*

Figure 4.1: Graphic representation of signal and normalization channels [36].

the other hand as input variable for the final fit (§4.5). Anyway, after all cleaning cuts, the signal to noise ratio amounts to $\sim 1/100$. In order to overcome this, is necessary to demonstrate that each background source can be precisely controlled and described by Monte Carlo templates (§4.7).

The first aim of this work of thesis is to understand the analysis steps and replicate the main ones (templates production and final fit). This was done to identify the key points, that need to be taken care of, in furtherance of a $\mathcal{R}_{D^*}$ analysis, as a function of $q^2 \equiv (p_B - p_{D^*})^2 = (p_\tau + p_{\nu_\tau})^2$.
Relating to this, preliminary tests have been done. They include:

- a fit on all data, excluding q^2 observable;
- fits in two different q^2 regions;
- training of a new Multivariate analysis and fit to all data.

These feasibility studies are topics of § 5.

4.1 Analysis Method

In order to measure the quantity:

$$\mathcal{R}_{D^*} = \frac{\mathcal{B}(B^0 \to D^{*-}\tau^+\nu_\tau)}{\mathcal{B}(B^0 \to D^{*-}\mu^+\nu_\mu)}, \tag{4.1}$$

we make use of the following decay topology for $B^0 \to D^{*-}\tau^+\nu_\tau$:

$$\begin{aligned} B^0 \to & D^{*-}\tau^+\nu_\tau \\ & \hookrightarrow \pi^+\pi^-\pi^+(\pi^0)\bar{\nu}_\tau \\ & \hookrightarrow \bar{D}^0\pi^- \\ & \hookrightarrow K^+\pi^-. \end{aligned} \tag{4.2}$$

so the visible final state consists of six tracks: two pions plus a kaon originating from the D^{*-} decay chain (which is fully reconstructed), and three charged pion pions ($3\pi \equiv \pi^+\pi^-\pi^+$) decaying from the τ^+. In addition, events compatible with $\tau^+ \to 3\pi\pi^0\bar{\nu}_\tau$ are included too, even if the calorimetric information are not sufficient to properly reconstruct the neutral pion, which de facto is undetected as well as the two neutrinos.

From an experimental point of view is more convenient to measure:

$$\mathcal{K}_{D^*} \equiv \frac{\mathcal{B}(B^0 \to D^{*-}\tau^+\nu_\tau)}{\mathcal{B}(B^0 \to D^{*-}3\pi)}, \tag{4.3}$$

because here the numerator (called *signal* hereafter) and the denominator (called *normalization* hereafter) have the same visible final signature (Fig. 4.1), so many systematic uncertainties cancel in the ratio. $\mathcal{R}_{D^*}$ can be written as:

$$\mathcal{R}_{D^*} = \mathcal{K}_{D^*} \times \frac{\mathcal{B}(B^0 \to D^{*-}3\pi)}{\mathcal{B}(B^0 \to D^{*-}\mu^+\nu_\mu)}, \tag{4.4}$$

where the last fraction is actually an external input for this analysis. Other external inputs are the branching ratios $\mathcal{B}(\tau^+ \to 3\pi\bar{\nu}_\tau)$ and $\mathcal{B}(\tau^+ \to 3\pi\pi^0\bar{\nu}_\tau)$. All these values are reported in Tab. 4.1. Finally $\mathcal{K}_{D^*}$ can be determined, according to:

$$\mathcal{K}_{D^*} = \left(\frac{N_{sig}}{\epsilon_{sig}\mathcal{B}(\tau^+ \to 3\pi\bar{\nu}_\tau)} + \frac{N_{sig0}}{\epsilon_{sig0}\mathcal{B}(\tau^+ \to 3\pi\pi^0\bar{\nu}_\tau)} \right) \frac{\epsilon_{norm}}{N_{norm}}, \tag{4.5}$$

where N_{sig}, N_{sig0} and N_{norm} are the yields extracted from data of the two signal channels and of the normalization mode; ϵ_{sig}, ϵ_{sig0} and ϵ_{norm} are their respective selection efficiencies, evaluated on Monte Carlo (MC) samples.

The measurement of the signal yield will be realized with a three dimensional fit to data. The three considered observables are: q^2, the τ^+ lifetime, together with the already cited output variable of a Multivariate Analysis. The fit model will be based on MC templates, validated and corrected by suitable control samples. The latter will be also exploited to estimate several background parameters, which will reduce the degrees of freedom in the final fit.

Channel	$\mathcal{B}(\%)$	Ref.
$B^0 \to D^{*-}\tau^+(\to 3\pi(\pi^0)\bar{\nu}_\tau)\nu_\tau$	0.173 ± 0.005	[13]
$\tau^+ \to 3\pi\bar{\nu}_\tau$	9.31 ± 0.05	
$\tau^+ \to 3\pi\pi^0\bar{\nu}_\tau$	4.62 ± 0.05	
$B^0 \to D^{*-}\mu^+\nu_\mu$	4.88 ± 0.10	[4]
$B^0 \to D^{*-}3\pi$	0.721 ± 0.029	
$B^0 \to D^{*-}3\pi(\pi^0)$	2.5 ± 0.3	
$B^0 \to D^{*-}D_s^+/D_s^{*+}/D_s^+(2317)/D_s^+(2457)(\to 3\pi)$	0.040 ± 0.004	
$B^0 \to D^{*-}D_s^+/D_s^{*+}/D_s^+(2317)/D_s^+(2457)(\to 3\pi)N$	0.56 ± 0.06	
$B^0 \to D^{*-}K^0D^{*+}(\to D^+(\to 3\pi(\pi^0))\gamma/\pi^0)$	0.0050 ± 0.0005	
$B^0 \to D^{*-}K^0D^+(\to 3\pi(N))$	0.0123 ± 0.0011	
$B^0 \to D^{*-}D^+(\to 3\pi(N))$	0.0012 ± 0.0001	
$B^0 \to D^{*-}K^0D^{*+}(\to D^0(\to K^-3\pi(\pi^0))\pi^+)$	0.067 ± 0.006	
$B^0 \to D^{*-}K^+D^{*0}(\to D^0(\to K^-3\pi(\pi^0))\gamma/\pi^0)$	0.130 ± 0.012	
$B^0 \to D^{*-}K^+D^0(\to K^-3\pi(\pi^0))$	0.030 ± 0.003	

Table 4.1: Branching fractions for the relevant channels of this analysis. Where not differently specified, PDG is assumed as reference [7]. In the first row, $\mathcal{B}$ for the signal channel is a Standard Model prevision.

4.2 First Backgrounds Overview

Several sources of background are considered. Each one is composed of many categories, which are here introduced and named.

The main channels, which produce the physical background, are listed in Tab. 4.1 with their branching fraction[2]. The table suggests that the more relevant component of the physical background will be due to $B^0 \to D^{*-}3\pi(N)$, called "prompt background" hereafter (N stands for a possible undetected neutral system). This component can be heavily suppressed, requiring that the decay vertex of the candidate τ^+ lepton is sufficiently downstream with respect to the decay vertex of the candidate B^0; we will refer to this as "detached-vertex cut". Furthermore, the latter can be upturned, thus producing a prompt-background control sample, which can be used to obtain N_{norm}.

After this selection, the physical background is due to candidates where the three pions originate from a particle of detectable lifetime. We will call it "double-charm" background. Specifically: $B^0 \to D^{*-}X_D(X)$ with $X_D \to 3\pi(N)$; here X_D stands for D_s^+, D^+, D^0, while (X) specifies that the inclusive modes are also considered. The main contribution is given by the D_s^+-mode. This background category has complicated possible resonance intermediate states, such as: D_s^{+*}, $D_{s0}^{+*}(2317)$, $D_{s1}^{+}(2460)$. Other similar and relevant, double-charm background channels are[3]: $B^{0,+} \to D^{**}D_s^+X$ and $B_s^0 \to D^{*-}D_s^+X$.

The others background categories are combinatorial. First of all, a wrong association may occur between a D^*-originated and a τ^+-originated decay chain: each of them can be correctly reconstructed, even if they are not daughters of the same b hadron[4]. The 3π system, in fact can stem from: a different B^0 mesons of the event ($B1B2$ category), the decay of charm hadrons produced at the PV (*charm* category), another PV, an interaction in the beam pipe or in the detector material; after cleaning cuts the $B1B2$ category is the more relevant. Moreover, a wrong tracks association may affect the single D^*-originated decay chain, even if the invariant mass distribution of these fully reconstructed decays should suppresses it ($notD^*$ category). Concerning instead the 3π candidate system, the combinatorial background regards essentially two pions, which originate from the same vertex, while the third one come from the primary vertex (PV), from a different vertex in the decay chain of the same b hadron, from a different b hadron or from a different PV.

[2] Three body decays such as $B \to D^*DK$ also exist: with exited kaons states (mostly $K^*(890)$), with excitations of the second D, or both. Anyway, these components involve, at least, two missing kaons plus several other neutral particles, coming from resonances de-excitation. As a result, the visible mass is smaller than the one expected for signal and so these modes do not represent a serious background for this analysis.

[3] With D^{**} we refer to all the already cited charmed resonances; as usual X indicates the inclusive modes.

[4] The low momentum of the pion emitted in the decay $D^{*-} \to \bar{D}^0\pi^-$ decreases precision in the determination of D^{*-} and B^0 decay vertex.

Variable	Cut	Targeted Background
$m(K^+\pi^-)$	$\in [1845, 1885]$ GeV/c^2	combinatorial
$p_T(\pi_s^-)$	> 0.11 GeV/c	combinatorial
$m(D^{*-}) - m(\bar{D}^0)$	$\in [143, 148]$ MeV/c^2	combinatorial
$[z(3\pi) - z(B^0)]/\sigma_{z(3\pi)-z(B^0)}$	> 4	prompt
$p_T(\pi)$	> 0.25 GeV/c	combinatorial
$m(3\pi)$	< 1.6 GeV/c^2	double-charm
$r_{3\pi}$	$\in [0.2, 0.5]$ mm	spurious 3π
$\chi^2_{IP}(\bar{D}^0)$	> 10	charm
$\chi^2_{IP}(\pi)$, π from 3π	> 15	combinatorial
$PV(\bar{D}^0)$	$= PV(3\pi)$	charm/combinatorial
number of B^0 candidates	$= 1$	all
3π vertex χ^2	< 10	combinatorial
BDT output	> -0.075	double-charm

Table 4.2: Selection cuts for signal sample. The table is subdivided according to text reference sections. Isolation requirements are not reported for brevity.

Finally, other possible sources of background may come from particle identification (PID); in particular $K-\pi$ or $e, \mu-\pi$ misidentification. LHCb PID performances manage to make negligible the second one.

4.3 Selection Criteria

This section describes the cuts applied to increase the signal purity. Tab. 4.2 and text summarise and explain the main requirements.

D^* reconstruction. The criteria are applied to the full D^{*-} decay chains. $\bar{D}^0$ candidates are reconstructed, requiring an invariant mass of the $K^+\pi^-$ pair to be between 1845 and 1885 MeV/c^2. These are combined with soft pions (π_s^-) of transverse momentum larger than 0.11 GeV/c, such that the difference between the D^{*-} and the $\bar{D}^0$ masses lies between 143 and 148 MeV/c^2.

4.3.1 Topological Requirements

The detached-vertex cut. According to MC, the mean longitudinal momentum of τ^+ leptons, created by $B^0 \to D^{*-}\tau^+\nu_\tau$ decays, is ~ 70 GeV in the laboratory frame. So their relativistic factor is $\gamma \approx 55$ and they fly on average for 5 mm in the beam pipe

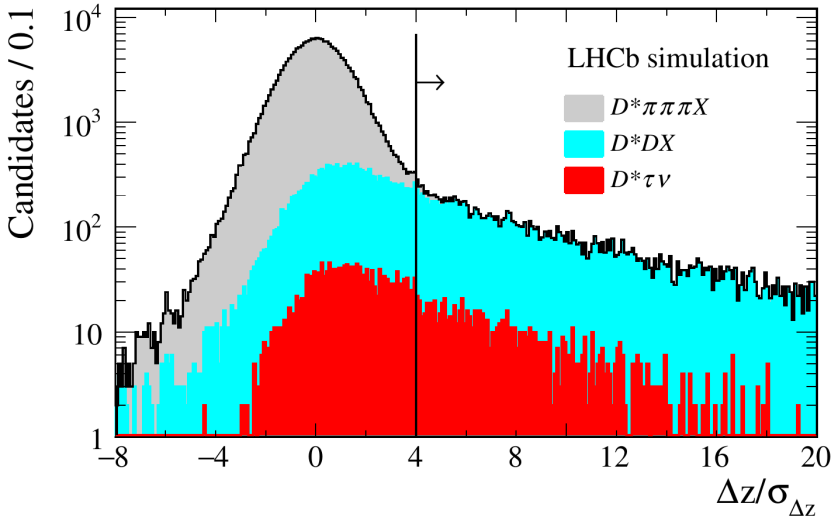

Figure 4.2: MC Distribution of the distance between the B^0 decay vertex and the 3π vertex along the beam direction, divided by its uncertainty. The gray area indicates the prompt background; the cyan area indicates the double-charm background; the red area indicates the signal. Histograms are not stacked. The vertical line shows the 4 σ cut used in the analysis.

before decaying[5]. This allow to select signal candidates with flight distance four times grater than its uncertainty, in the beam direction. Studies on inclusive MC simulations show that this detched-vertex requirement reduces the prompt background of more than three order of magnitude. On the other side, only 10% of the signal events survives after this cut. Fig. 4.2 graphically displays the effectiveness of the requirement. Basically, the drawback on signal is fully compensated by a strong improvement in the sample purity. From the same figure we can also deduce the dominance of the double-charmed background over signal after this topological cut. Fig. 4.3 presents the invariant mass distribution of the 3π system after the vertex-detached cut; peaking structures due to $D_s^+ \to 3\pi$ and to $D^+ \to 3\pi$ are clearly visible.

Other topological cuts. In order to suppress combinatorial and charm backgrounds, in addition to the detached-vertex criterion, other cuts are implemented and reported in Tab. 4.2. These include a good track quality and a minimum transverse momentum of 250 MeV/c for each π. For 3π system a good vertex reconstruction quality and a large χ^2_{IP} with respect to any PV, are required; here χ^2_{IP} is defined as the difference in the vertex-fit χ^2 of a given PV reconstructed with and without the particle under consideration. The 3π invariant mass is required to be lower than 1.6 GeV/c^2 to reduce

[5]The lifetime of the tau lepton is $(290.3 \pm 0.5) \times 10^{-15}$s [7].

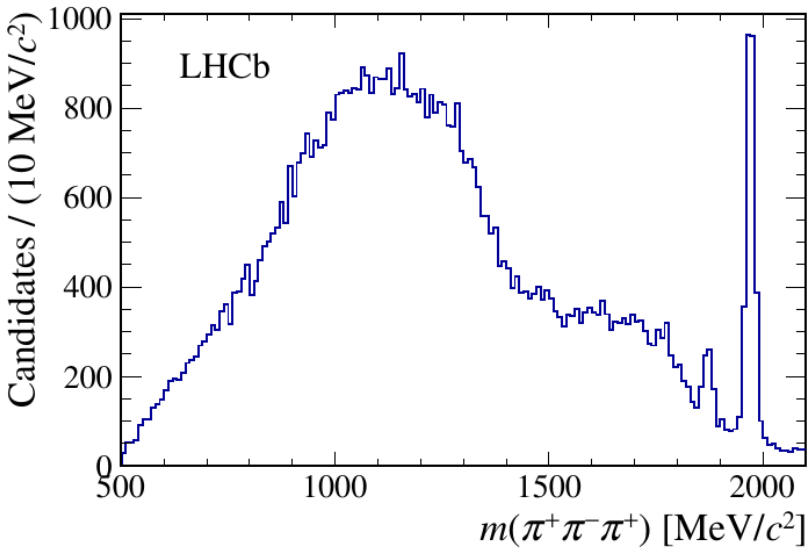

Figure 4.3: 3π invariant mass after detached-vertex requirement. D^+ and D_s^+ signal are visible in the spectrum [13].

double-charm background (see Fig. 4.3). Moreover, it is necessary to check that other protons interactions or secondary interactions with the beam pipe material do not generate the 3π system. To do that, the distance, $r_{3\pi}$, from the beam center and the 3π vertex must guarantee that the latter is neither inside the the beam envelope, nor outside the beam pipe.

4.3.2 Isolation Requirements

Charged isolation. In order to ensure that no extra charged tracks are compatible with B^0 or 3π decay vertices, a specific algorithm has been implemented. It counts the overall number of charged tracks having p_T larger than 250 MeV/c, $\chi^2_{IP} > 4$ with respect to the PV and χ^2_{IP} smaller than 25 with respect to the 3π and the B^0 vertex. If any such track is found, the candidate $D^{*-}3\pi$ is rejected.
The present strategy is particularly useful for discriminating double-charm physical background where a flying D^0 decays to $K^-3\pi(X)$.

Neutral isolation. Many background channels contains neutral particles in their decay chain. By virtue of that, they can be suppressed profiting by the energy deposited in the electromagnetic calorimeter. A pseudocone in $\Delta\eta - \Delta\phi$ of 0.3 units around the direction of the 3π system is taken as region of interest. Candidates are rejected if here the energy deposition exceeds 8 GeV.
This algorithm is indicated to discriminate against inclusive D_s^+ decays to $3\pi X$, which

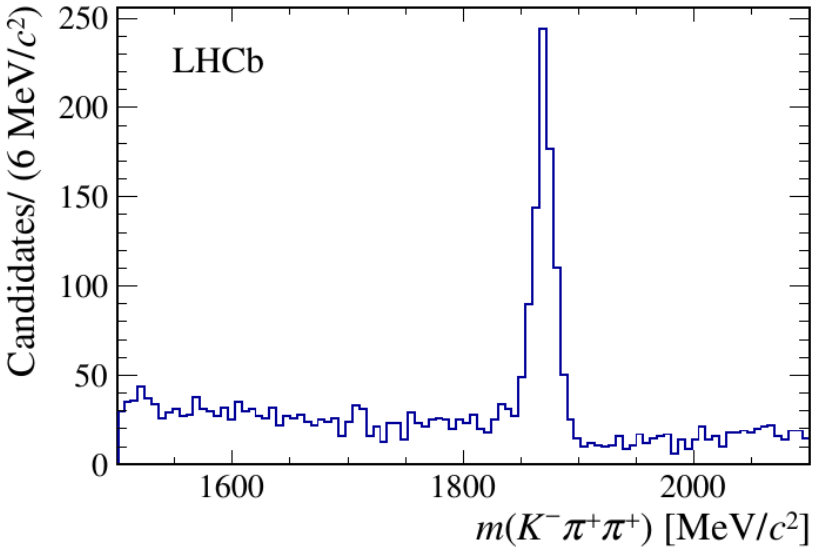

Figure 4.4: Spectrum of the $K^-\pi^+\pi^+$ invariant mass for candidates passing the signal selection, where the negative pion has been identified as a kaon and assigned the kaon mass [13].

contain photons or π^0 in addition to the three pions; photons are also produced when the D_s^+ excited states decay to their ground state. The drawback is that this strategy affects signal too. In fact, it vetoes $\tau^+ \to 3\pi\pi^0\bar{\nu}_\tau$ decays; their efficiency is roughly a half with respect to the 3π mode.

4.3.3 Particle identification requirements

The kaon identification probability of the soft pions was chosen to be less than 50%, in order to ensure a high efficiency in D^{*-} reconstruction. On the contrary more selective criteria was applied on the tracks forming the 3π candidate: kaon identification probability less than 17% for each positive candidate. Concerning the π^-, instead, the double-charm background $B^0 \to D^{*-}D^+X$ must be considered, in order to get better performances. In fact, the channels $D^+ \to K^-\pi^+\pi^+$ and $D^+ \to K^-\pi^+\pi^+\pi^0$ have large branching fraction, so this background contribution becomes important when the K^- is mis-identified as a π^-. Fig. 4.4 shows the $K^-\pi^+\pi^+$ invariant mass spectrum for candidates that have passed all analysis requirements, except that the π^- candidate must have a kaon identification probability above 88%. A clear D^+ peak can be seen, with little combinatorial background. As a result, the requirement on π^- candidates is a kaon identification probability below 12%.

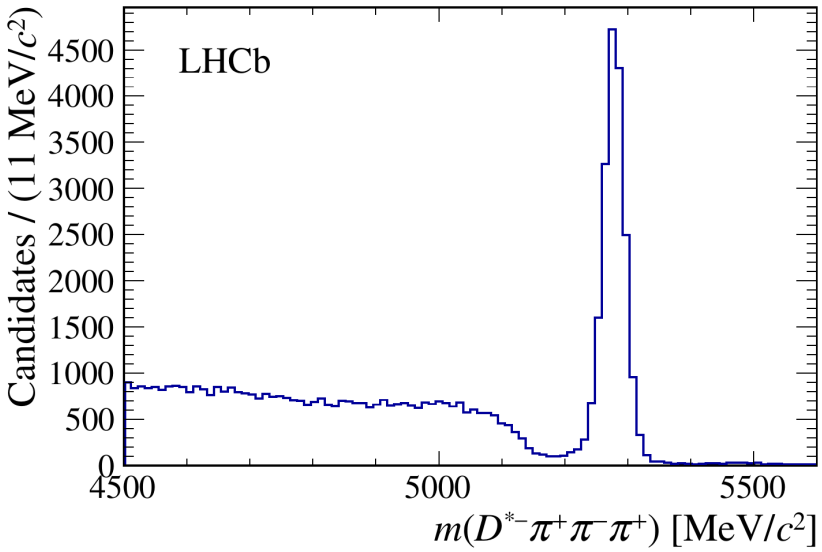

Figure 4.5: $D^{*-}3\pi$ invariant mass for the normalization sample [13].

4.3.4 Selection of the normalization channel

The $B^0 \to D^{*-}3\pi$ normalization channel is selected requiring the $\bar{D}^0$ decay vertex to be located at least 4 σ downstream of the 3π vertex along the beam direction. Moreover the $D^{*-}3\pi$ invariant mass distribution is cut around B^0 mass, namely between 5150 and 5400 MeV/c^2. The latter distribution is displayed in Fig. 4.5.

4.3.5 Selection efficiencies

This set of topological, isolation and PID criteria compose the analysis selection. Together with the BDT cut, which will be explained in the following, they produce the final samples, when applied on data, and the final templates, when applied on MC simulations. No BDT cut is applied to the normalization sample.
LHCb collaboration has tested the impact of each cut using MC simulations validated on specific data sample [13]. The results are listed in Tab. 4.3

4.4 Reconstruction of the decay kinematics

Reconstruction of signal. The presence of two undetectable neutrinos in the signal decay chain does not allow the proper and complete reconstruction of the events. Nevertheless, getting sufficiently precise estimations is still possible. In fact, the missing information can be recovered employing the known masses of B^0 and τ^+, together with their lines of flight, *i.e.* unit vectors joining the B^0 vertex to the PV and the 3π vertex

Category	Absolute efficiencies			Relative efficiencies		
	$D^{*-}3\pi$	$D^{*-}\tau^+\nu_\tau$		$D^{*-}3\pi$	$D^{*-}\tau^+\nu_\tau$	
		$3\pi\bar{\nu}_\tau$	$3\pi\pi^0\bar{\nu}_\tau$		$3\pi\bar{\nu}_\tau$	$3\pi\pi^0\bar{\nu}_\tau$
Geometrical acceptance:	14.65	15.47	14.64			
After:						
initial selection	1.382	0.826	0.729			
spurious 3π removal	0.561	0.308	0.238	40.6	37.3	32.6
trigger requirements	0.484	0.200	0.143	86.3	65.1	59.9
vertex selection	0.270	0.0796	0.0539	55.8	39.8	37.8
charged isolation	0.219	0.0613	0.0412	81.2	77.0	76.3
BDT cut	-	0.0541	0.0292	-	94.1	74.8
PID requirements	0.136	0.0392	0.0216	65.8	72.4	74.1

Table 4.3: Summary of the selection efficiencies (in %).

to the B^0 vertex, respectively. In these terms the τ^+ momentum in the laboratory frame is:

$$|\vec{p}_\tau| = \frac{(m_{3\pi}^2 + m_\tau^2)|\vec{p}_{3\pi}|\cos\theta_{\tau,3\pi} \pm E_{3\pi}\sqrt{(m_\tau^2 - m_{3\pi}^2)^2 - 4m_\tau^2|\vec{p}_{3\pi}|^2\sin^2\theta_{\tau,3\pi}}}{2(E_{3\pi}^2 - |\vec{p}_{3\pi}|^2\cos^2\theta_{\tau,3\pi})}, \tag{4.6}$$

where $\theta_{\tau,3\pi}$ is the angle between the 3π system three-momentum and the τ line of flight (Fig. 4.6); $m_{3\pi}$, $|\vec{p}|_{3\pi}$ and $E_{3\pi}$ are the invariant mass, three-momentum and energy of the 3π system, respectively; m_τ is the known τ^+ mass. In principle, $\theta_{\tau,3\pi}$ can be extracted from data, like the other parameters. However, equation (4.6) shows a two fold ambiguity. In order to overcome it, a good choice is to consider $\theta_{\tau,3\pi}$ maximum value:

$$\theta_{\tau,3\pi}^{\max} = \arcsin\left(\frac{m_\tau^2 - m_{3\pi}^2}{2m_\tau|\vec{p}_{3\pi}|}\right); \tag{4.7}$$

if we assume the approximation $|\vec{p}_\tau| = |\vec{p}_\tau(\theta_{\tau,3\pi}^{\max})|$, the ambiguity disappears. The same leads to the estimation of the B^0 momentum:

$$|\vec{p}_{B^0}| = \frac{(m_Y^2 + m_{B^0}^2)|\vec{p}_Y|\cos\theta_{B^0,Y} \pm E_Y\sqrt{(m_{B^0}^2 - m_Y^2)^2 - 4m_{B^0}^2|\vec{p}_Y|^2\sin^2\theta_{B^0,Y}}}{2(E_Y^2 - |\vec{p}_Y|^2\cos^2\theta_{B^0,Y})}, \tag{4.8}$$

and:

$$\theta_{B^0,Y}^{\max} = \arcsin\left(\frac{m_{B^0}^2 - m_Y^2}{2m_{B^0}|\vec{p}_Y|}\right). \tag{4.9}$$

Here Y stands for the $D^{*-}\tau^+$ system: its momentum, energy and mass can be calculated using the previous estimation of $\vec{p}_\tau$:

$$\vec{p}_Y = \vec{p}_{D^*} + \vec{p}_\tau, \quad E_Y = E_{D^*} + E_\tau, \quad m_Y = \sqrt{E_Y^2 - |\vec{p}_Y|^2}. \tag{4.10}$$

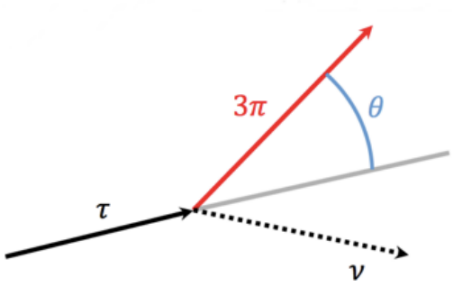

Figure 4.6: Proper definition of $\theta_{\tau,3\pi}$. In the analysis its maximum value, allowed by kinematics, is used instead.

The uncertainty caused by these approximations can be tested using MC simulations. Fig. 4.7 shows the difference between the reconstructed and the true square of the 4-momentum transferred, *i.e.* $q^2 \equiv (p_{B^0} - p_{D^*})^2 = (p_\tau + p_{\nu_\tau})^2$. A resolution of 1.2 GeV^2/c^4 is obtained, while no significant bias is observed.

Reconstruction of double-charm candidates. After the detached-vertex requirement, the main source of background is originated by decays of the form: $B \to D^{*-} D_s^+ (X)$, with $D_s^+ \to 3\pi N$; here N is a system of unreconstructed neutral particles, which cause a lack of information in the event description. However, the measure of the B^0 and D_s^+ lines of flight, together with the known B^0 mass are sufficient to obtain an estimation of the kinematics of these decays.

Adopting the notation of Fig. 4.8, a possible strategy basically works as follow. First of all, momentum conservation and vectorial algebra tell us that the momenta $\vec{p}_B$ and $\vec{p}_{D_s^+}$ can be estimated measuring: the D^* momentum ($\vec{p}_{D^*}$) which is fully reconstructed, and mesons lines of flight ($\hat{u}_B$, $\hat{u}_{D_s^+}$,). As first approximation $\hat{u}_{D_s^+}$ can be estimated with the flight direction of the 3π system, namely ignoring other possible neutral particle in D_s^+ decay. Nevertheless, to get a better precision, one must consider that the B^0 decay vertex is not so well reconstructed because of the low momentum of the soft pion coming from $D^{*-} \to \bar{D}^0 \pi_s^-$ decay. Corrections to the B^0 vertex location can be applied, using its correlation with the 3π invariant mass, namely MC extracted information. Further calculus details are not indispensable here and can be found in [13]; in latter reference is also shown that the above introduced corrections essentially do not affect the B^0 vertex location resolution, but slightly reduce its bias.

In conclusion, the observables reconstructed in the double-charm hypothesis will be included among the input variables of the Multivariate Analysis (MVA) illustrated in section 4.5.

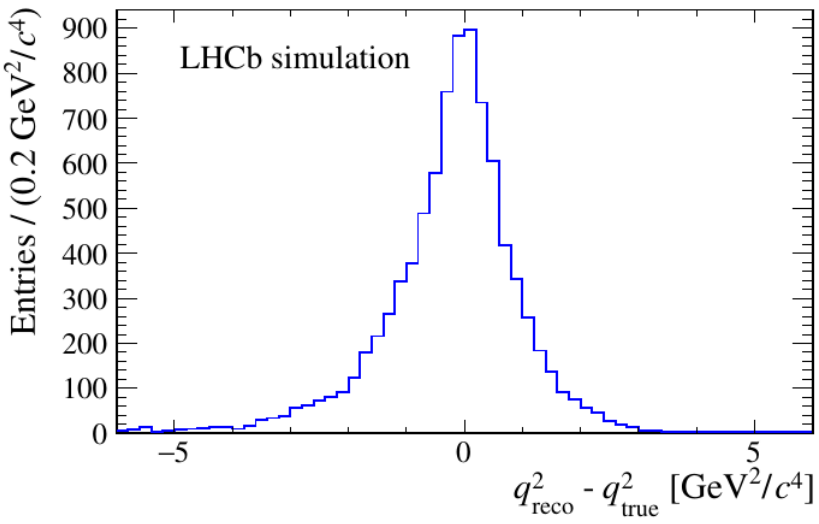

Figure 4.7: Difference between the reconstructed and the true q^2, obtained by MC simulation of the signal channel [13].

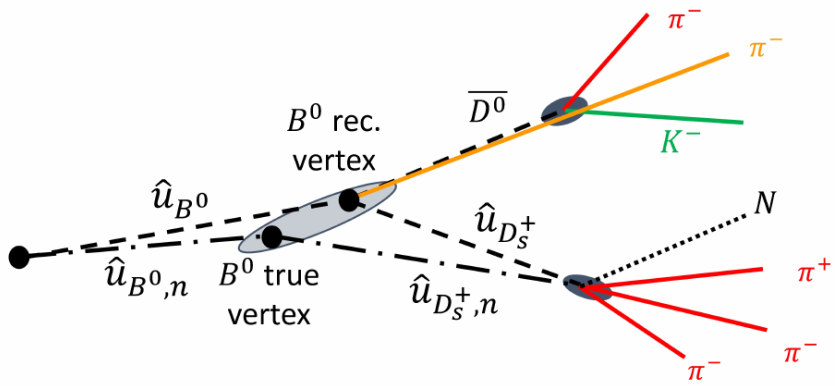

Figure 4.8: Scheme of the decay topology in the double-charm hypothesis.

4.5 Multivariate Analysis

In order to reject the double-charm background, three features can be used:

- the different resonant structures of $\tau \to 3\pi\bar{\nu}_\tau$ and $D_s \to 3\pi X$ decays;
- the neutral isolation;
- the different kinematic properties of signal and background candidates.

Thus a Multivariate Analysis, based on Boosted Decision Trees (BDT), was implemented[6]. It combines 18 variables; among them: the output variables of the neutral isolation algorithm; momenta, invariant masses and quality of the reconstruction of the decay chain under the signal and background hypotheses; the invariant masses of oppositely charged pions, the energy and the flight distance in the transverse plane of the 3π system; the invariant mass of the six charged tracks.

The BDT was trained using MC samples of signal and double-charm background decays. Signal events with $\tau^+ \to 3\pi\pi^0\bar{\nu}_\tau$ were actually excluded from training. In fact, they decrease BDT discrimination performances, because the neutral isolation variables for this kind of signal are very similar to the background ones.

Fig. 4.9 shows the normalized distributions of the four input variables having the largest discriminating power, namely: the minimum and maximum of the invariant masses of oppositely-charged pions, ($\min[m(\pi^+\pi^-)]$ and $\max[m(\pi^+\pi^-)]$); the neutrino energy, approximated as $|\vec{p}_{B^0}| - (|\vec{p}_{D^*}| + |\vec{p}_\tau|)$ in the signal hypothesis; and the $D^{*-}3\pi$ invariant mass. The BDT response for signal and background test samples is illustrated in Fig. 4.10.

In order to enhance purity, the value -0.075 of the BDT output variable was chosen as threshold for data: events with a lower output were cut from the analysis sample and reused to create a D_s-enriched control sample.

4.6 Determination of the signal yield: fit strategy

The yield of $B^0 \to D^{*-}\tau^+\nu_\tau$ decays is determined from a three-dimensional binned maximum likelihood fit to the distributions of q^2, τ^+ decay time (t_τ or `TauCTAU`) and BDT output (`BDT`); the number of bins are 8, 8, 4 respectively. The probability density function (*pdf*) for each component of signal and background was deduced from the relative MC simulation. The value of each *pdf*, in each bin, is the number of corresponding MC events, in the corresponding bin, normalized to the total events number of the same simulation for the various component, signal and background included in the fit. This technique is

[6] It was done exploiting the methods of `TMVA4` [37]

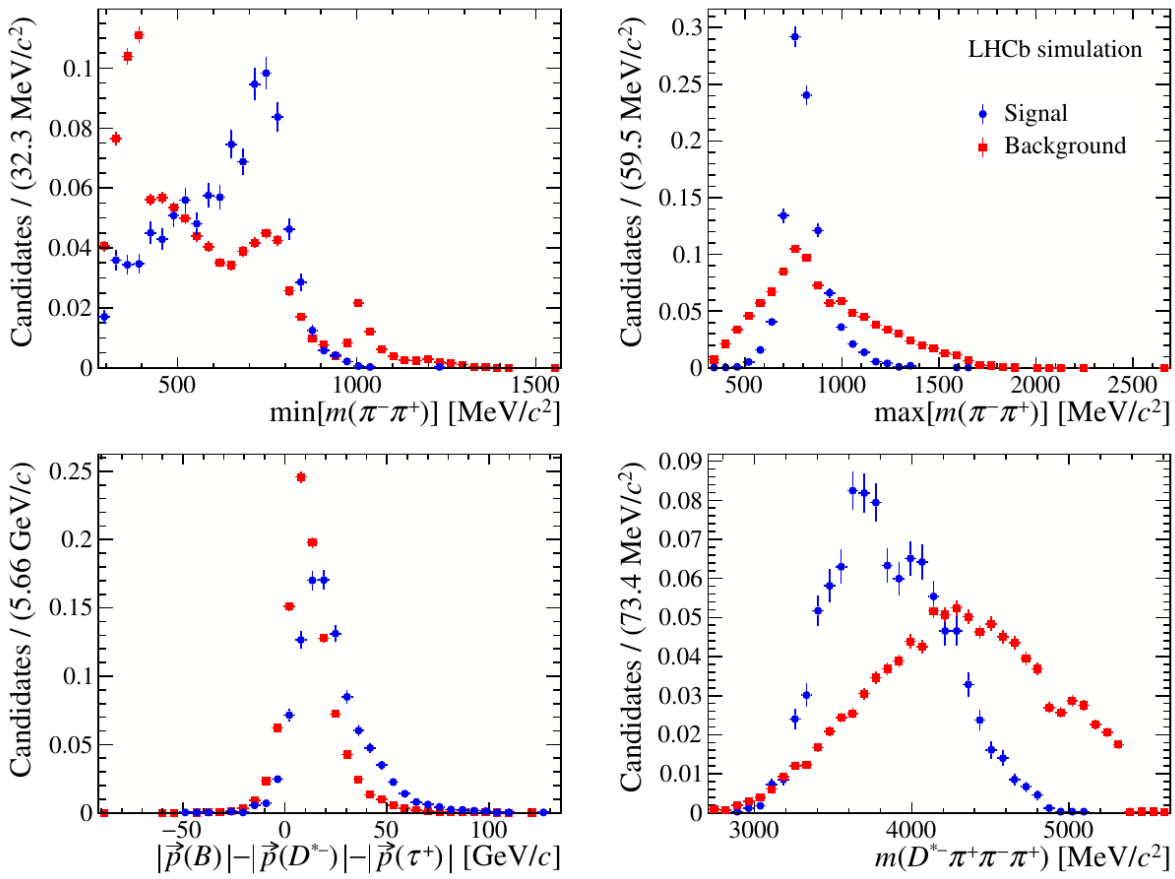

Figure 4.9: Normalized distribution of the best discriminating input variables of the BDT [13].

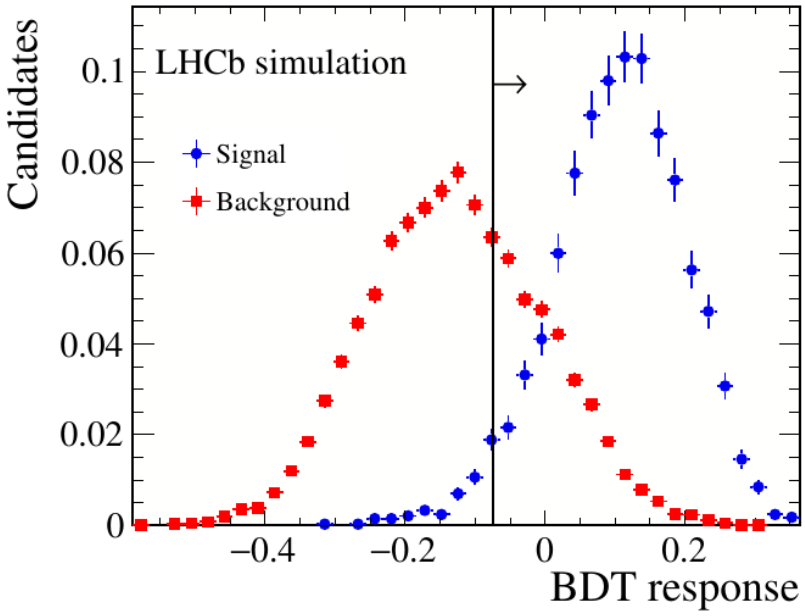

Figure 4.10: BDT response to signal and background test samples [13].

usually called "production of templates", where a template corresponds to an histogram of a certain component (signal or background). The fit model can be written as:

$$\mathcal{P}(q^2, t_\tau, \texttt{BDT}; \vec{\theta}) = \sum_i N_i h_i(q^2, t_\tau, \texttt{BDT}), \tag{4.11}$$

where the sum covers all templates, h_i, and their normalization factors N_i. The association between the i^{th} template and the corresponding physical channel is reported in Tab. 4.4. The same table shows the structure of the normalization factors, as functions of the final fit parameters, some of them free to vary in the likelihood minimization, other fixed from external inputs. The fit procedure includes: free parameters, fixed parameters, but also parameters with a Gaussian constraint. The free parameters are: the yield of signal candidates N_{sig}; the yields of event involving a D_s^+, N_{D_s}; the yield of event involving a D^+, N_{D^+}; the fraction of D^0 combinatorial event, f_{D0}^{v1v2} (see §4.7.3). The following sections will introduce the fixed and the constrained parameter, explaining their physical meaning. Auxiliary studies are required to get and set all these values; they exploit theory notions, MC predictions and comparisons with control samples obtained from data. Other ancillary, but crucial, studies regard the validation and correction of template shapes. These latter parts of the main analysis were not directly replicated in this work of thesis, for which they are, in fact, external inputs (coming from [13]); however, they are important steps, that need to be understood in order to consciously implement the rest, so we report them here anyway. The final results of the fit procedure

i	**Physical Channel**	**Normalization** (N_i)
1	$B^0 \to D^{*-}\tau^+(\to 3\pi\bar{\nu}_\tau)\nu_\tau$	$N_{sig} \times f_{\tau\to 3\pi\nu}$
2	$B^0 \to D^{*-}\tau^+(\to 3\pi\pi^0\bar{\nu}_\tau)\nu_\tau$	$N_{sig} \times (1 - f_{\tau\to 3\pi\nu})$
3	$B \to D^{**}\tau^+\nu_\tau$	$N_{sig} \times f_{D^{**}\tau\nu}$
4	$B^0 \to D^{*-}D_s^+$	$N_{D_s} \times f^1_{D_s}/k$
5	$B^0 \to D^{*-}D^*_{s0}(2317)^+$	$N_{D_s} \times f^2_{D_s}/k$
6	$B^0 \to D^{*-}D_{s1}(2460)^+$	$N_{D_s} \times f^3_{D_s}/k$
7	$B^{0,+} \to D^{**}D_s^+X$	$N_{D_s} \times f^4_{D_s}/k$
8	$B_s^0 \to D^{*-}D_s^+X$	$N_{D_s} \times f^5_{D_s}/k$
9	$B^0 \to D^{*-}D_s^{*+}$	$N_{D_s} \times 1/k$
10	$B \to D^{*-}D^0X$ same vertex	N_{D^0}
11	$B \to D^{*-}D^0X$ different vertices	$N_{D^0} \times f^{v1v2}_{D^0}$
12	$B \to D^{*-}D^+X$	N_{D^+}
13	$B \to D^{*-}3\pi X$	$N_{B\to D^{*-}3\pi X}$
14	$B1B2$ combinatorics	N_{B1B2}
15	Combinatoric D^{*-}	N_{notD^*}

Table 4.4: Summary of fit components with their normalization parameters. $k \equiv \sum_j f^j_{D_s}$

will be presented in §4.8.

4.7 Parameters estimation and Templates re-weigthing

4.7.1 Signal parameters

The signal is composed by two components. We call $f_{\tau\to 3\pi\nu_\tau}$ the fraction of $\tau \to 3\pi\nu_\tau$ signal candidates with respect to the sum of the $\tau \to 3\pi\nu_\tau$ and $\tau \to 3\pi\pi^0\nu_\tau$ components. This parameter is fixed to 0.78 in the final fit, according to the different branching fractions (see Tab. 4.1) and efficiencies of the two modes (ϵ_{sig}, ϵ_{sig0} see Tab. 4.3).

$$f_{\tau\to 3\pi\nu_\tau} = \frac{\epsilon_{sig}\mathcal{B}(\tau \to 3\pi\nu_\tau)}{\epsilon_{sig}\mathcal{B}(\tau \to 3\pi\nu_\tau) + \epsilon_{sig0}\mathcal{B}(\tau \to 3\pi\pi^0\nu_\tau)} = 0.78. \tag{4.12}$$

Furthermore we introduce here $f_{D^{**}\tau\nu}$, which is the ratio of the yield of $B \to D^{**}\tau\nu_\tau$ decay candidates to the signal decays. Its value is fixed in the final fit: $f_{D^{**}\tau\nu} = 0.11$. This result is essentially a theory prediction [38], corrected by the selection efficiency of this channel extracted using the relative MC simulation.

4.7.2 The D_s^+ background

As already explained, the main physical background arise because of real D_s^+ mesons exchanged for τ^+ leptons. As introduced in section 4.2, many modes contribute to this category:

$$\begin{array}{lll} 1)\ B^0 \to D^{*-} D_s^+; & 2)\ B^0 \to D^{*-} D_{s0}^*(2317)^+; & 3)\ B^0 \to D^{*-} D_{s1}(2460)^+; \\ 4)\ B^{0,+} \to D^{*-} D_s^+ X; & 5)\ B_s^0 \to D^{*-} D_s^+ X; & 6)\ B^0 \to D^{*-} D_s^{*+}. \end{array} \tag{4.13}$$

Moreover, studies on MC indicatesthat this double-charm background will overwhelm signal by two order of magnitude. Therefore, it is of primary importance not only to control the MC predictions about the relative decay rate of the modes in (4.13), but also to check the simulated decay model for $D_s^+ \to 3\pi(X)$; [7] The next two paragraphs show that deviations from simulations were found in both cases. In order to correct them: (i) an appropriate weight, deduced in the first test, will be applied to each MC event, thus producing a re-shaping of the templates, (ii) fractions $f_{D_s}^j$ are straightforwardly assumed from the second test.

The D_s^+ decay model

The branching fraction $\mathcal{B}(D_s^+ \to 3\pi)$ is 15 times smaller than the exclusive one $\mathcal{B}(D_s^+ \to 3\pi X)$ [13]. This is due to large contributions from intermediate states, R, such as K_s^0, η, η', ϕ, ω. The branching fraction for processes of the type $D_s^+ \to R\pi^+$ are well known, while large uncertainties are still present for channels such as $D_s^+ \to R(\to \pi^+\pi^- X)\pi^+\pi^0$ or $D_s^+ \to R3\pi$ [7]. This lack of knowledge affects the MC simulations. Thus a parallel analysis was conducted by LCHb collaboration. In brief: the $B \to D^{*-} D_s^+(X)$ control sample, obtained from data requiring a low BDT output, was used for a simultaneous fit on four observables: $\min[m(\pi^+\pi^-)]$, $\max[m(\pi^+\pi^-)]$, the invariant mass of the same-charge pions, $m(\pi^+\pi^+)$, and the invariant mass of the 3π system, $m(3\pi)$. The fit model was composed of templates, whose shape was taken from MC simulation; basically four main categories were considered:

- D_s^+ decays where at least one pion originates from the decay of a η meson;
- D_s^+ decays similar to the precedent ones, but with a η';
- D_s^+ decays where at least one pion originates from an intermediate state different from η and η' (mainly ω and ϕ);
- other D_s^+ decay, where none of the three pions originates from an intermediate resonance.

[7] Basically, we have to study the resonance intermediate states which originate not only at the D_s^+ production vertex, but also at his decay vertex.

D_s^+ decay	Relative contribution	Correction to simulation
$\eta\rho^+$	0.109 ± 0.016	0.88 ± 0.13
$\eta\pi^+$	0.047 ± 0.014	0.75 ± 0.23
$\eta'\rho^+$	0.179 ± 0.016	0.710 ± 0.063
$\eta'\pi^+$	0.135 ± 0.015	0.808 ± 0.088
$\phi\rho^+$	0.043 ± 0.021	0.28 ± 0.14
$\phi\pi^+$	0.163 ± 0.021	1.588 ± 0.208
$\eta 3\pi$	0.104 ± 0.021	1.81 ± 0.36
$\eta' 3\pi$	0.0835 ± 0.0102	5.39 ± 0.66
$\omega 3\pi$	0.0415 ± 0.0122	5.19 ± 1.53
$K^0 3\pi$	0.0204 ± 0.0139	1.0 ± 0.7
$\phi 3\pi$	0.141 ± 0.021	0.97
$\tau^+(\to 3\pi(N)\bar{\nu}_\tau)\nu_\tau$	0.0135	0.97
3π non-resonant	0.038 ± 0.005	6.69 ± 0.94

Table 4.5: Results of the fit to the D_s^+decay model. For each channel the relative contribution together with its correction to the simulation yield are reported.

Any category actually contained several subcategories; the fit procedure managed to estimate the relative contribution of each one. Fig. 4.11 shows the plots with the final model superimposed on the fitted data. Tab. 4.5 lists the relative contribution of each D_s^+ decay mode. These results, corrected for the different efficiency in the high BDT region, are exploited to upgrade the shape of the templates used in the final fit. Basically, in MC we know for each event the true, i.e. simulated, resonance decay scheme that produced it; so in order to get better relative fractions between modes, each event enters in the histogram that produce the relative templates with a weight; the weight brought by each event is the ratio of its fitted relative contribution (Tab. 4.5, second column) to the original relative contribution, corrected for efficiency[8]. For this analysis is particularly significant the η' contribution. This because among τ^+ hadronic decays is relevant $\tau^+ \to a_1(1260)^+\nu_\tau$ (see [7]) and then a_1 resonance produces $\rho^0\pi^+$ final states. Concerning D_s^+ decays, the first source of ρ^0 is actually: $\eta' \to \rho^0\gamma$.

[8]The option "re-do all the simulations with better decay fractions" was not at hand for questions of calculus time.

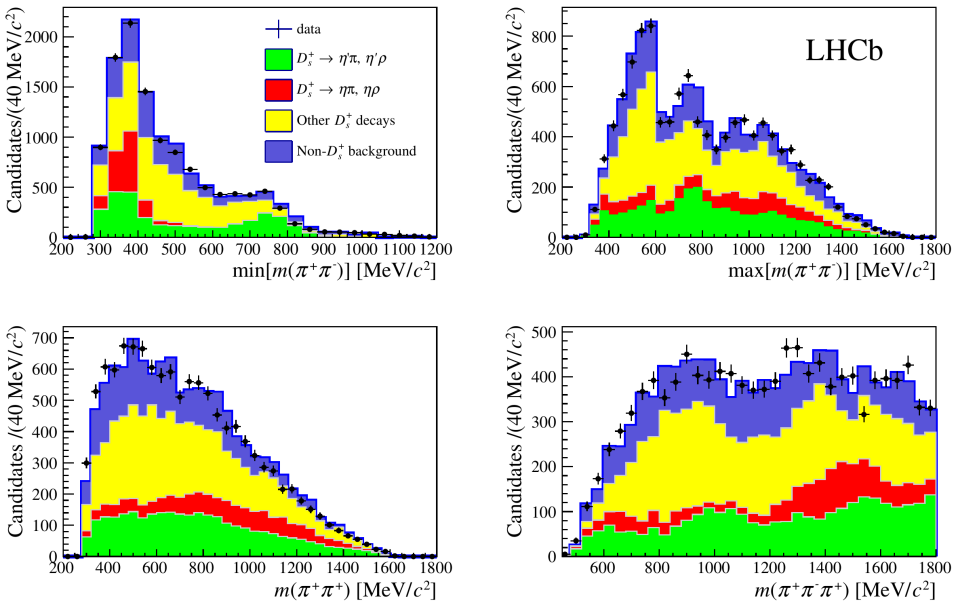

Figure 4.11: Fit for the D_s^+ decay model. Data from the $B^{\to}D^{*-}D_s^+(X)$ enriched control sample and model are superimposed. Legend links the four shown components to the ones described in the text [13].

Estimation of $f^i_{D_s}$

In order to check the relative contribution of each mode in $B \to D^{*-}D_s^+(X)$ a control sample, obtained requiring exclusive $D_s^+ \to 3\pi$ decays[9], can be used. A fit to the invariant mass spectrum of the $D^{*-}3\pi$ system is then performed through the model:

$$\mathcal{P} = f_{WS}\mathcal{P}_{WS} + (1 - f_{WS}) \sum_{i=1}^{6} \frac{f^i_{D_s}\mathcal{P}_i}{\sum_{j=1}^{6} f^j_{D_s}}, \tag{4.14}$$

where: $f^i_{D_s}$ is the fraction of events of the i^{th} mode in (4.13) with respect to the 6^{th} mode (of course $f^6_{D_s} = 1$); $\mathcal{P}_i$ is the template for the mode i: its shape is taken from simulation; $\mathcal{P}_{WS}$ is the template for the combinatorial background: its shape is taken from another control sample, called "Wrong Sign", where the D^{*+} meson and the 3π system have the same charge; f_{WS} is the relative fraction of the combinatorial background. The fit results are shown in Fig. 4.12 and reported in Tab. 4.6, where a comparison with the corresponding values in the simulation is also given, along with their ratios. Fractions $f^i_{D_s}$, together with their uncertainties and correlations (Tab. 4.7), are used to constrain D_s^+ contributions in the final fit.

[9]Essentially the difference with respect to the analysis selection is that now $m(3\pi) \in [1939, 1999]$ GeV/c^2. Of course the BDT cut is inverted too. Is is also assumed that these cuts do not affect the relative fractions of the $B \to D^{*-}D_s^+(X)$ components [13].

i	Parameter	Simulation	Fit	Ratio
	f_{WS}		0.014	
1	$f_{D_s^+}$	0.54	0.585 ± 0.041	1.08 ± 0.07
2	$f_{D_{s0}^{*+}}$	0.08	0.000 ± 0.019	0.00 ± 0.24
3	$f_{D_{s1}^+}$	0.39	0.364 ± 0.052	0.93 ± 0.13
4	f_{D_sX}	0.22	0.399 ± 0.069	1.81 ± 0.31
5	$f_{D_sX,s}$	0.23	0.095 ± 0.028	0.41 ± 0.12

Table 4.6: Relative fractions for the components of $B \to D^{*-} D_s^+(X)$. The values used in the simulation, the fit results and the ratio of the two are reported. The table introduces a more explicit notation for the fractions.

	$f_{D_s^+}$	$f_{D_{s0}^{*+}}$	$f_{D_{s1}^+}$	f_{D_sX}	$f_{D_sX,s}$
$f_{D_s^+}$	1	0.001	0.159	−0.184	0.071
$f_{D_{s0}^{*+}}$	0.001	1	−0.002	0.000	0.001
$f_{D_{s1}^+}$	0.159	−0.002	1	0.600	0.424
f_{D_sX}	−0.184	0.000	0.600	1	0.552
$f_{D_sX,s}$	0.071	0.001	0.424	0.552	1

Table 4.7: Correlation between the components of the $B \to D^{*-} D_s^+(X)$ control sample. The used notation is introduced in Tab. 4.6.

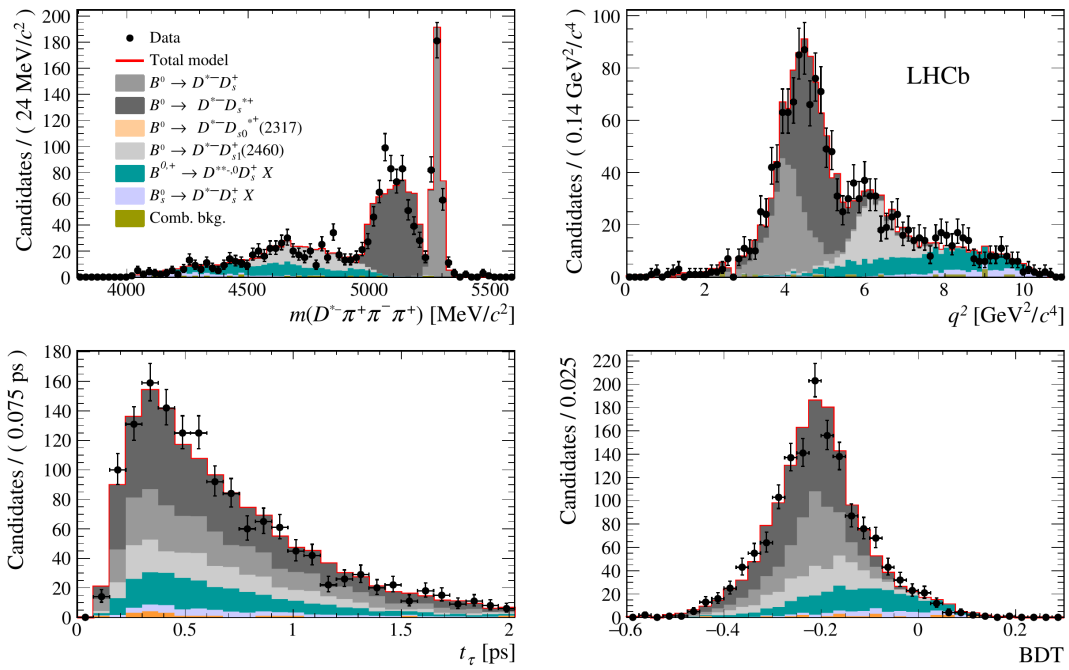

Figure 4.12: Data and final model for the fit to the $B \to D^{*-}D_s^+(X)$ control sample. The distributions for the final fit variables are also shown as cross check.

4.7.3 The D^0 and D^+ backgrounds

The main channels for D^0 and D^+ decays into final states with three pions can synthetically be written as: $D^{0,+} \to K^{-,0}3\pi(\pi^0)$. Their subresonant structure are known quite well, however a slight disagreement between data and simulation was found for both cases.

Concerning the D^0 case, a control sample was built, using the charged isolation tool to select a candidate K^- compatible with an origin from the 3π vertex and such as the invariant mass of the $K^-3\pi$ system is consistent with the known D^0 mass. A detailed study proposed in [13] reports difference between data and simulation relatively to the distribution of q^2 and $m(D^{*-}D^0)$; by virtue of that, MC events were re-weighted, to get better spectra.

As already proposed in section 4.3.3, a control sample for $B \to D^{*-}D^+(X)$ decays can be obtained inverting the PID requirement for the negative pion in the 3π system and selecting events in the D^+ peak. The limited size of the obtained control sample did not allow to determine specific correction to MC distribution, even if disagreement with data was found. In first approximation it has been chosen to apply to the template of this background component the same re-weighting deduced from the $B \to D^{-*}D^0(X)$ control sample. This can be justified noticing that the dominant decay has the structure

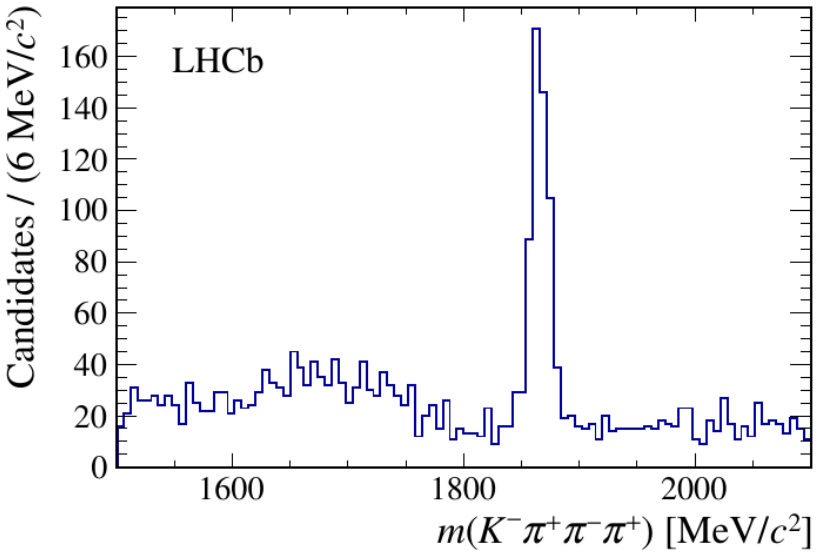

Figure 4.13: Distribution of $m(K^-3\pi)$ for candidates were a charged kaon is associable to the 3π vertex.

$B \to D^{*-}DK$ for both cases ($D = D^0, D^+$).

Estimation of N_{D^0}. The $B \to D^{-*}D^0(X)$ control sample permits to estimate the expected yield of the corresponding background component in the data sample. In particular, it was done getting a statistical estimation of the number of events which compose the D^0 peak in $K^-3\pi$ invariant mass distribution (Fig. 4.13).
After a proper correction for the different selection efficiencies between data sample and control sample, it was found:

$$N_{D^0} = 444 \pm 22, \tag{4.15}$$

where the 5% relative uncertainty essentially accounts for the efficiency in finding the additional kaon. This result was used to introduce a Gaussian constraint in the final fit.

Introduction of f_{D0}^{v1v2}. A sort of combinatorial background for the $B \to D^{*-}D^0(X)$ channel exists. It is in fact possible to reconstruct events where at least one pion originates from the D^0 vertex and the other pion(s) from a different vertex. This is the case when the soft pion from a D^{*-} decay is reconstructed as it were produced at the 3π vertex. This circumstance is encoded in the final fit with an adequate template and a floating parameter f_{D0}^{v1v2}, namely the ratio between the yield for this kind of events and N_{D^0}.

4.7.4 The $B \to D^{*-}3\pi(X)$ yield

The yield of the prompt background component ($B \to D^{*-}3\pi(X)$) can be predicted basically using the normalization sample as pure control sample of exclusive $B \to D^{*-}3\pi$ decays; if N_{exc}^{norm} is the number of events which compose it, an estimation of the inclusive prompt yield is given by:

$$N_{inc} = N_{exc}^{norm} \frac{N_{inc}^{MC}}{N_{exc}^{MC}} \epsilon, \tag{4.16}$$

where $N_{inc}^{MC}/N_{exc}^{MC}$ is the ratio between the inclusive and exclusive prompt yields taken from simulations, while ϵ accounts for the different selection efficiency between signal and normalization samples. The final result is:

$$N_{B \to D^* 3\pi X} \equiv N_{inc} = 443 \pm 21. \tag{4.17}$$

This numbers will rule a Gaussian constraint in the final fit.

4.7.5 Yields for the combinatorial background

The templates for two kind of combinatorial background are included in the final fit. The first one is the $B1B2$ category. Even if the WS control sample is available, its shape is deduced from the inclusive $D^*3\pi X$ Monte Carlo. In fact, $B \to D^*(D_s \to 5\pi)X$ decays contaminate WS control sample in the low region of $m(D^*3\pi)$. Vice versa, comparing the WS control sample to data, we can see that combinatorial background dominates when $m(D^*3\pi) > 5.1$ Gev/c^2 (Fig. 4.14). Thus the number of event in this region was used to rescale and fix the normalization of the $B1B2$ template:

$$N_{B1B2} = \frac{N_{B1B2}^{MC}}{N_{B1B2}^{MC}(m(D^*3\pi) > 5.1)} N^{data}(m(D^*3\pi) > 5.1) = 197. \tag{4.18}$$

The second combinatorial category included in the fit is the $notD^*$ one. Its yield can be fixed using the number of event in the $\bar{D}^0$ mass sidebands from the $D^{*-} \to \bar{D}^0\pi_s^-$ decay. The result is:

$$N_{notD*} = 243. \tag{4.19}$$

4.8 Fit Results

The fit results produced by this work of thesis are consistent with data and with the preliminary result found by LHCb collaboration [13]; they are compared in Tab. 4.8. In Fig. 4.15 and Fig. 4.16 the data are superimposed on the final model. In conclusion the signal yield found by this work of thesis is:

$$N_{sig} = 1326 \pm 95. \tag{4.20}$$

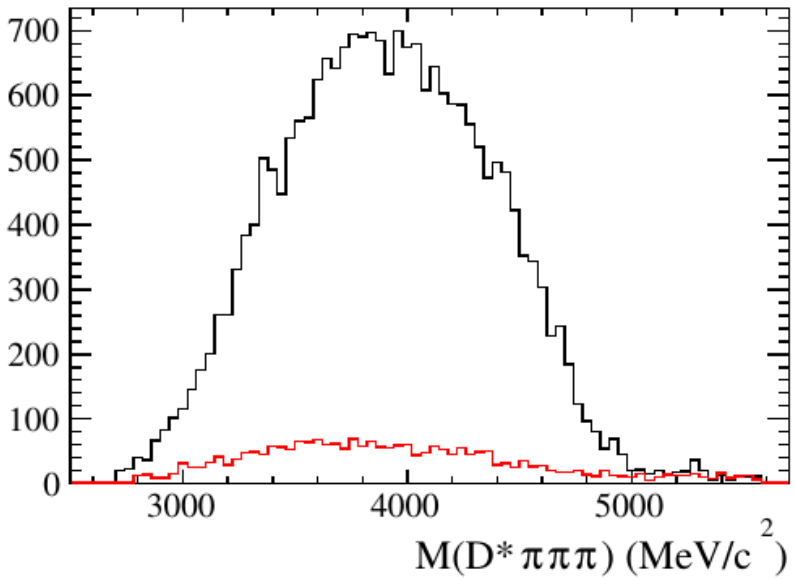

Figure 4.14: $m(D^*3\pi)$ distribution form data (black) and WS control sample (red); the histograms are not re-normalized [39].

The aim of this analysis is to reproduce the published results in order to deeply understand the complicated fitting model. This step is essential in order to further develop the model towards the measurement of $\mathcal{R}_{D^*}$ as function of q^2, as described in the following sections.

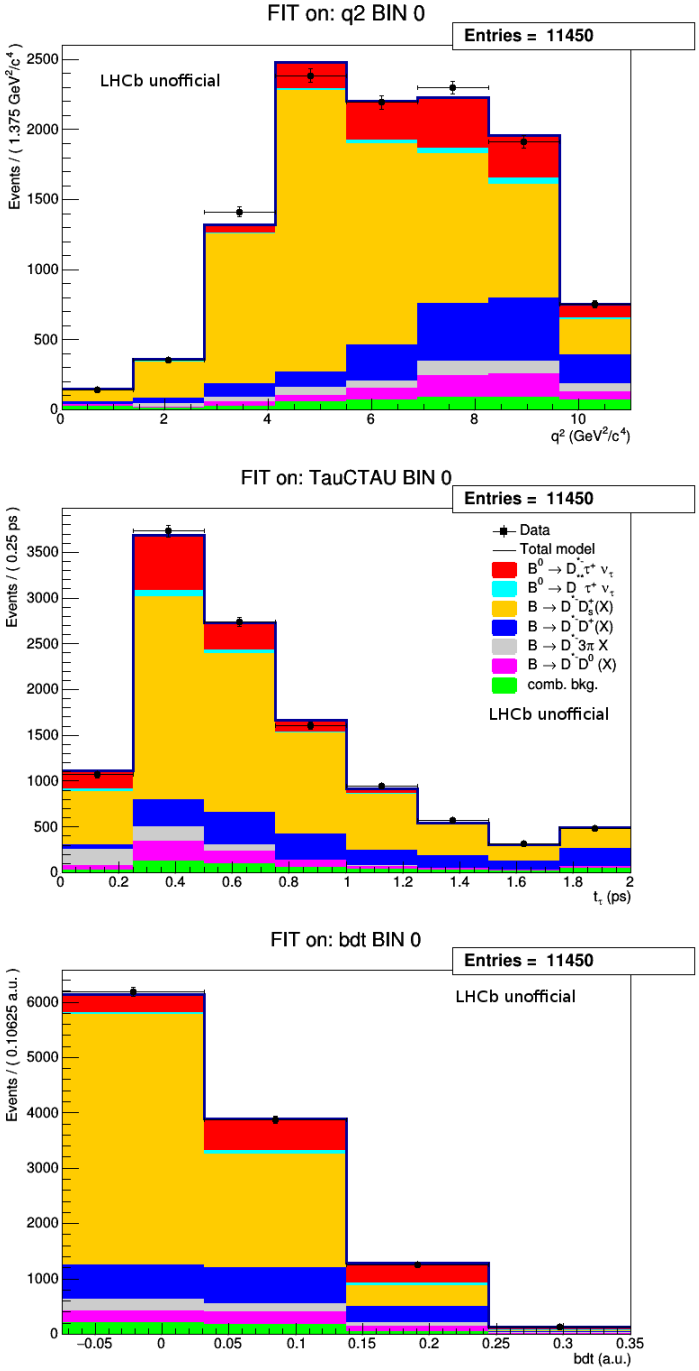

Figure 4.15: Projections of the three-dimensional fit on the (top) q^2 , (middle) τ^+ decay time and (bottom) BDT output distributions. Legend identifies the various components.

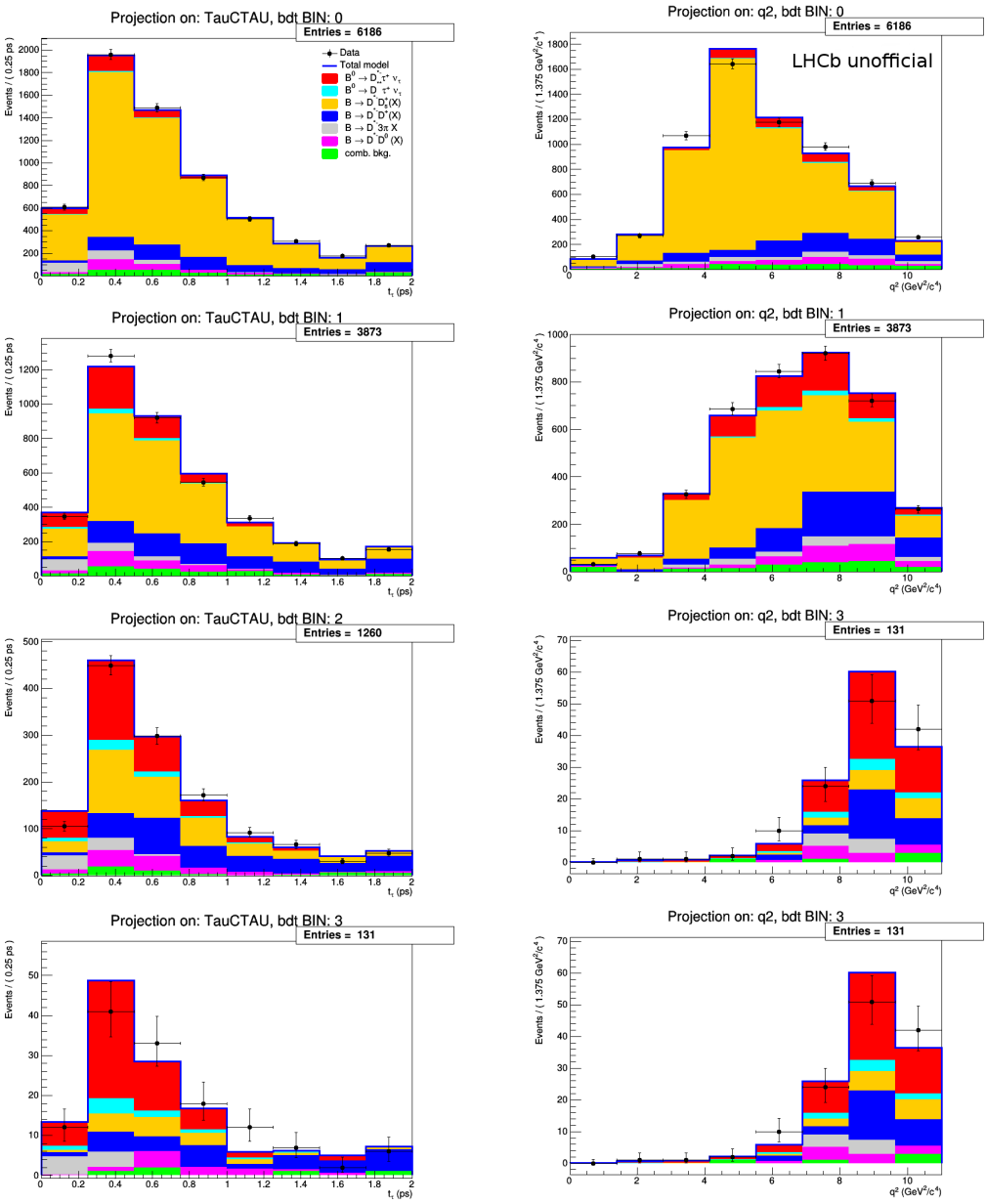

Figure 4.16: Projections on the (left) τ^+ decay time and (right) q^2 distributions for the four BDT bins. The highest BDT bin is associated to the two lower plots.

Parameter	This Thesis Results	Constraints	Reference Results[13]
N_{sig}	1326 ± 95		1313 ± 95
$f_{\tau \to 3\pi\nu}$	0.78	0.78 (fixed)	0.78
$f_{D^{**}\tau\nu}$	0.11	0.11 (fixed)	0.11
N_{D^+}	1688 ± 115		1624 ± 152
$N_{D^0}^{SV}$	445 ± 22	445 ± 22	444 ± 22
$f_{D^0}^{v1v2}$	0.42 ± 0.22		0.28 ± 0.23
N_{D_s}	6829 ± 174		6972 ± 187
$f_{D_s^+}$	0.474 ± 0.033	0.460 ± 0.032	0.474 ± 0.032
$f_{D_{s0}^{*+}}$	-0.019 ± 0.018	0.000 ± 0.019	0 ± 0.008
$f_{D_{s1}^+}$	0.454 ± 0.036	0.437 ± 0.062	0.444 ± 0.039
f_{D_sX}	0.739 ± 0.045	0.635 ± 0.110	0.792 ± 0.057
$f_{D_sX,s}$	0.196 ± 0.023	0.144 ± 0.042	0.224 ± 0.031
$N_{B\to D^{*-}3\pi X}$	425 ± 21	443 ± 22	424 ± 21
N_{B1B2}	197	197 (fixed)	197
N_{notD^*}	243	243 (fixed)	243

Table 4.8: Fit result for the three-dimensional fit.

Chapter 5

Toward $\mathcal{R}_{D^*}(q^2)$

As shown by equation (2.10), the Standard Model is able to calculate $\mathcal{R}_{D^*}$ as a function of the 4-momentum transferred to the leptonic part of the decay. However, any experimental measurement has finite q^2 resolution and it is done in a finite q^2 range. Therefore, our results are actually compared to:

$$\mathcal{R}^{SM}_{D^*} = \frac{\int_{q^2_{min}}^{q^2_{max}} \frac{d\Gamma_\tau}{dq^2}\, dq^2}{\int_{q^2_{min}}^{q^2_{max}} \frac{d\Gamma_\ell}{dq^2}\, dq^2} \qquad (\text{with: } \ell = e, \mu), \tag{5.1}$$

where $d\Gamma_{\tau,\ell}/dq^2$ come from (2.3). The prediction (2.11) is actually obtained in this way, namely integrating on all q^2 range allowed by kinematic: $q^2_{min} = m^2_\tau \approx 3$ GeV^2/c^4, $q^2_{min} = (m_{B^0} - m_{D^{*-}})^2 \approx 11$ GeV^2/c^4. This is in fact the range were signal was found. New Physics may provoke deviations from $\mathcal{R}^{SM}_{D^*}$ that cancel themselves in the integral, *i.e.* deviations may be enhanced if we analyse many smaller q^2 ranges. We will call them "q^2 bins". In principle, the smaller the q^2 bins are, the better test on (2.10) we do.

From a statistical point of view, these ideas throw in two problems:

a) we may have not collected yet enough data, in each q^2 bin, to produce statistically significant measurements;

b) we must avoid hypothesises related with SM prediction of q^2 distribution, at least for signal.

Observation (b) implies that is necessary to avoid use the q^2 variable from simulated MC events and that all q^2-dependent signal variables should be not used, especially to build the `BDT` observable.

In order to upgrade what learned by the analysis of the precedent chapter, we realized the task of "$\mathcal{R}_{D^*}$ in q^2 bins" through subsequent tests:

1) fit in all q^2 range, using t_τ and `BDT` observables (§5.1);

2) fit in two q^2 ranges ($q^2 \gtrless 5.5$ GeV^2/c^4), using just t_τ and BDT observables (§5.2);

3) training of a new MVA classifier with input variable independent from the q^2 and fit in the full q^2 range, using the distributions of q^2, t_τ and the output variable of the new classifier, BDTG (§5.3).

Even if this is not the final fit, which foresees to fit data with t_tau and BDTG in bins of q^2, it is an essential step in order to reproduce the published results. The following sections will illustrate in detail each step, together with results.

5.1 Fit 2D unbinned

Since we are no more allowed to exploit the q^2 distribution, the very first preliminary test consists in verifying whether the fit model, implemented in the previous chapter, is able to discriminate signal and background, just without using this variable. Technically this means to create two-dimensional templates, *i.e.* translating in *pdf* two-dimensional histograms with just t_τ and BDT as inputs. All other features of the fit model are left untouched, so we can still refer to (4.11) and Tab. 4.4; the only change is $h_i(q^2, t_\tau, \texttt{BDT}) \rightarrow h_i(t_\tau, \texttt{BDT})$.

The fit results are listed in the third column of Tab. 5.1. Fig. 5.1 and Fig. 5.2 display data and the model fitted to them. The signal yield now found is:

$$N_{sig}^{(2D)} = 1227 \pm 141, \tag{5.2}$$

to be compared to $N_{sig}^{3D} = 1326 \pm 95$. As expected we obtain larger statistical uncertainties, but the results are compatible even if to conclude this a toy MC study is necessary, due to the different models adopted. The same is true also for all other fit results. No relevant discrepancies are observed between the plots (Fig.s 4.15-4.16 vs. Fig. 5.1-5.2).

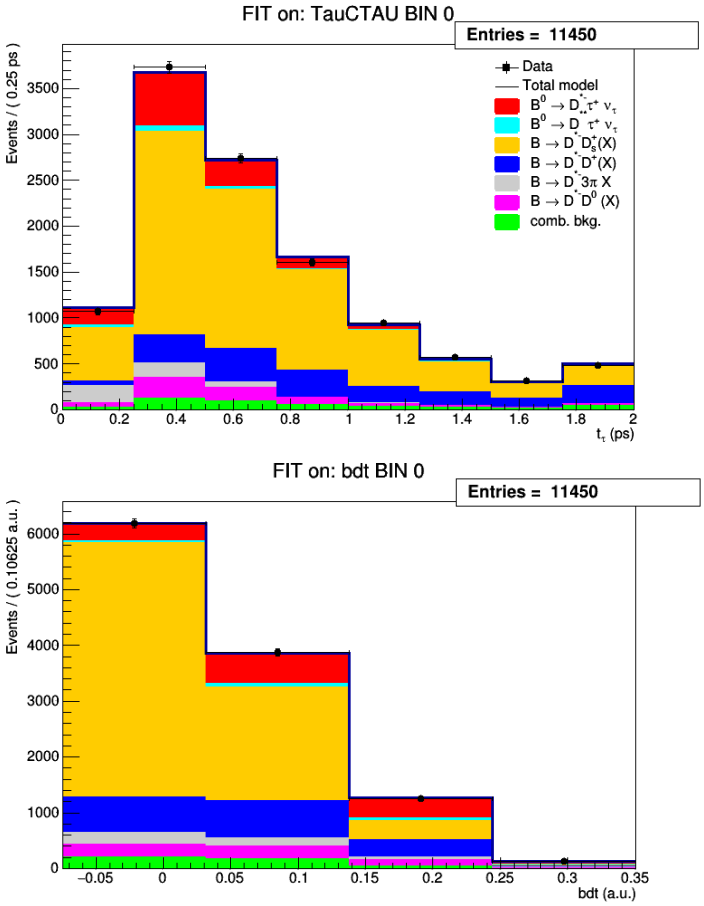

Figure 5.1: Projections of the two-dimensional fit on the (top) τ^+ decay time and (bottom) BDT output distributions. Legend identifies the various components.

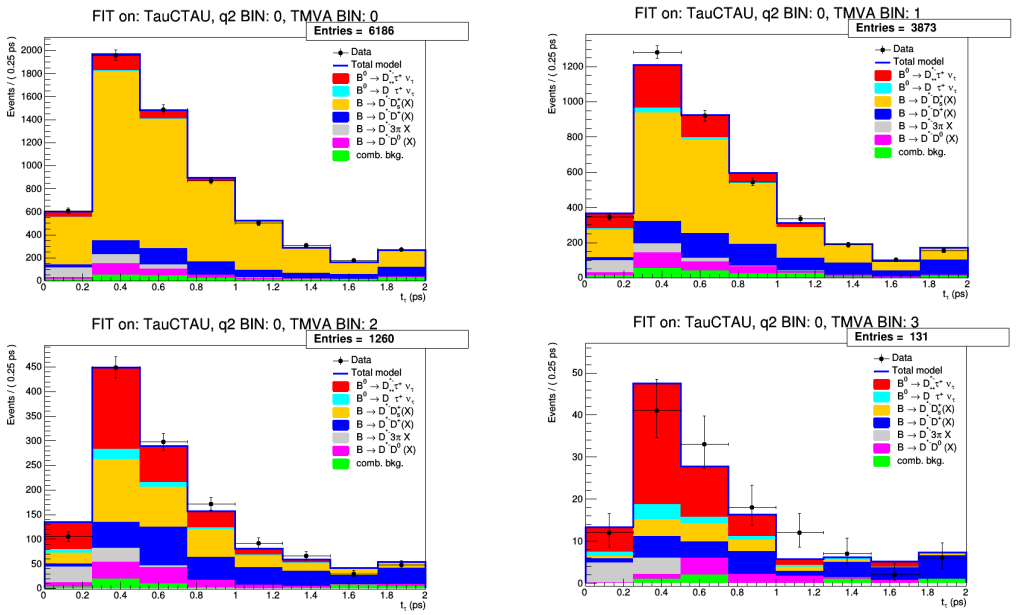

Figure 5.2: Projections of the two-dimensional fit on the τ^+ decay time for the four BDT bins.

Parameter	**Constraints**	**Fit 3D** $(q^2, t_\tau, \texttt{BDT})$	**Fit 2D** $(t_\tau, \texttt{BDT})$	**Fit 3D** $(t_\tau, \texttt{BDTG})$
N_{sig}		1326 ± 95	1227 ± 141	1560 ± 92
$f_{\tau\to 3\pi\nu}$	0.78 (fixed)	0.78	0.78	0.78
$f_{D^{**}\tau\nu}$	0.11 (fixed)	0.11	0.11	0.11
N_{D^+}		1688 ± 115	1678 ± 139	1767 ± 112
$N_{D^0}^{SV}$	445 ± 22	445 ± 22	449 ± 22	446 ± 27
$f_{D^0}^{v1v2}$		0.42 ± 0.22	0.58 ± 0.61	0.00 ± 0.04
N_{D_s}		6829 ± 174	6833 ± 269	6727 ± 160
$f_{D_s^+}$	0.460 ± 0.032	0.474 ± 0.033	0.444 ± 0.040	0.48 ± 0.03
$f_{D_{s0}^{*+}}$	0.000 ± 0.019	-0.019 ± 0.018	-0.001 ± 0.019	0.002 ± 0.016
$f_{D_{s1}^+}$	0.437 ± 0.062	0.454 ± 0.036	0.453 ± 0.051	0.35 ± 0.03
f_{D_sX}	0.635 ± 0.110	0.739 ± 0.045	0.684 ± 0.065	0.81 ± 0.07
$f_{D_sX,s}$	0.144 ± 0.042	0.196 ± 0.023	0.162 ± 0.027	0.19 ± 0.03
$N_{B\to D^*-3\pi X}$	443 ± 22	425 ± 21	434 ± 22	411 ± 21
N_{B1B2}	197 (fixed)	197	197	197
N_{notD^*}	243 (fixed)	243	243	243

Table 5.1: Comparison of fit results of the three tests executed in the full q^2 range.

5.2 Fit 2D binned

The second test consists in re-doing twice what shown in the previous section: above and below the threshold $q^2 = 5.5$ GeV^2/c^4. Thus, the fit model can be written in the synthetic form (4.11), for each q^2 bin. Event with $q^2 < 5.5$ GeV^2/c^4 form the dataset of the first q^2 bin, the others fill the dataset of the second q^2 bin. By analogy, the simulated events with $q^2 \gtrless 5.5$ GeV^2/c^4 are used to produce the templates that are going to fit the correspondent dataset[1].

The main change, introduced in this test, concerns the unfitted values of fixed and constrained parameters: the introduced q^2 requirement is supposed to modify them. We faced this question exploiting the MC predictions. Each fixed or constrained parameter is related to the yield of the correspondent signal or background component. We can use MC to estimate the selection efficiency of each q^2 bin and then get all the needed corrections. The same reasoning can be also exploited to estimate reference values of the free parameters in each q^2 bin; now the starting values are the results of the three-dimensional fit (Tab. 4.8). In this way we get reference values for each parameter of each bin. Tab. 5.2 lists the used formulas. In the table ϵ_i^n is the ratio between number of simulated events in the q^2 bin and the total number of simulated event,for each component i.

The fit results are listed in Tab. 5.3 for both q^2 bins. Fig. 5.3 and Fig. 5.4 display data and the model fitted to them for the first q^2 bin; Fig. 5.5 and Fig. 5.6 do the same for the second one. The signal yields found are:

$$\begin{aligned} N_{sig}^{(1)} &= 370 \pm 60 \qquad \text{if: } 0 < q^2 < 5.5 \text{ GeV}^2/\text{c}^4; \\ N_{sig}^{(2)} &= 930 \pm 100 \qquad \text{if: } 5.5 < q^2 < 11 \text{ GeV}^2/\text{c}^4. \end{aligned} \tag{5.3}$$

to be compared to $N_{sig}^{(1)} = 272 \pm 20$ and $N_{sig}^{(2)} = 1041 \pm 74$, as explained above.

[1] For the moment, we skip any consideration about correlations with q^2. They will be topic of next section. Now we just want to preliminary check, whether each q^2 bin has enough statistic to go ahead.

i	**Physical Channel**	**Correction Formula**
1	$B^0 \to D^{*-}\tau^+(\to 3\pi\bar{\nu}_\tau)\nu_\tau$	$f^{(n)}_{\tau\to 3\pi\nu} = \frac{\epsilon^n_1 f_{\tau\to 3\pi\nu}}{\epsilon^n_1 f_{\tau\to 3\pi\nu}+\epsilon^n_2(1-f_{\tau\to 3\pi\nu})}$
2	$B^0 \to D^{*-}\tau^+(\to 3\pi\pi^0\bar{\nu}_\tau)\nu_\tau$	$N^{(n)}_{sig} = N^{(3D)}_{sig}(\epsilon^n_1 f_{\tau\to 3\pi\nu} + \epsilon^n_2(1 - f_{\tau\to 3\pi\nu}))$
3	$B \to D^{**}\tau^+\nu_\tau$	$f^{(n)}_{D^{**}\tau\nu} = \frac{\epsilon^n_3 f_{D^{**}\tau\nu}}{\epsilon^n_1 f_{\tau\to 3\pi\nu}+\epsilon^n_2(1-f_{\tau\to 3\pi\nu})}$
4	$B^0 \to D^{*-}D^+_s$	$f^{1(n)}_{D_s} = \epsilon^n_4 f^1_{D_s}/\epsilon^n_9$
5	$B^0 \to D^{*-}D^*_{s0}(2317)^+$	$f^{2(n)}_{D_s} = \epsilon^n_5 f^2_{D_s}/\epsilon^n_9$
6	$B^0 \to D^{*-}D_{s1}(2460)^+$	$f^{3(n)}_{D_s} = \epsilon^n_6 f^3_{D_s}/\epsilon^n_9$
7	$B^{0,+} \to D^{**}D^+_s X$	$f^{4(n)}_{D_s} = \epsilon^n_7 f^4_{D_s}/\epsilon^n_9$
8	$B^0_s \to D^{*-}D^+_s X$	$f^{5(n)}_{D_s} = \epsilon^n_8 f^5_{D_s}/\epsilon^n_9$
9	$B^0 \to D^{*-}D^{*+}_s$	$(f^{6(n)}_{D_s} = 1)$ $N^{(n)}_{D^+_s} = N_{D^+_s}(\sum_{j=1}^6 \epsilon_{j+3} f^j_{D_s})/(\sum_{j=1}^6 f^j_{D_s})$
10	$B \to D^{*-}D^0X$ same vertex	$N^{(n)}_{D^0} = \epsilon^n_{10} N_{D^0}$
11	$B \to D^{*-}D^0X$ different vertices	$f^{v1v2(n)}_{D^0} = \epsilon^{(n)}_{11} f^{v1v2}_{D^0}/\epsilon^{(n)}_{10}$
12	$B \to D^{*-}D^+X$	$N^{(n)}_{D^+} = \epsilon^n_{12} N_{D^+}$
13	$B \to D^{*-}3\pi X$	$N^n_{B\to D^{*-}3\pi X} = \epsilon^n_{13} N_{B\to D^{*-}3\pi X}$
14	$B1B2$ combinatorics	$N^{(n)}_{B1B2} = \epsilon^n_{14} N_{B1B2}$
15	Combinatoric D^{*-}	$N^{(n)}_{notD^*} = \epsilon^n_{15} N_{notD^*}$

Table 5.2: Fraction efficiency correction for each q^2 bin.

Parameter	$\boldsymbol{q^2}$ **bin: 1** ($0 < q^2 < 5.5$ GeV^2/c^4)		$\boldsymbol{q^2}$ **bin: 2** ($5.5 < q^2 < 11$ GeV^2/c^4)	
	Expec. Value	Fit Result	Expec. Value	Fit Result
$f_{\tau\to 3\pi\nu}$	0.81	0.81	0.77	0.77
$f_{D^{**}\tau\nu}$	0.06	0.06	0.12	0.12
N_{B1B2}	75	75	197	197
N_{notD^*}	46	46	122	122
$f_{D_{s1}^+}$	0.130 ± 0.018	0.139 ± 0.018	1.7 ± 0.2	1.6 ± 0.2
$f_{D_s^+}$	0.491 ± 0.034	0.49 ± 0.03	0.33 ± 0.02	0.326 ± 0.003
$f_{D_{s0}^{*+}}$	0.000 ± 0.013	-0.002 ± 0.013	0.00 ± 0.04	0.00 ± 0.04
f_{D_sX}	0.107 ± 0.019	0.108 ± 0.019	2.7 ± 0.5	2.9 ± 0.4
$f_{D_sX,s}$	0.012 ± 0.004	0.012 ± 0.003	0.6 ± 0.2	0.81 ± 0.19
$N_{D^0}^{SV}$	83 ± 4	83 ± 4	362 ± 18	365 ± 18
$N_{B\to D^{*-}3\pi X}$	127 ± 6	126 ± 6	316 ± 15	312 ± 16
$f_{D^0}^{v1v2}$	0.15 ± 0.08	0.2 ± 0.7	0.311 ± 0.02	0.31 ± 0.06
N_{D^+}	266 ± 20	157 ± 52	1357 ± 102	1500 ± 140
N_{D_s}	3645 ± 96	3402 ± 110	3327 ± 87	3500 ± 300
N_{sig}	272 ± 20	370 ± 60	1041 ± 74	930 ± 100

Table 5.3: Fit results in the two q^2 bins

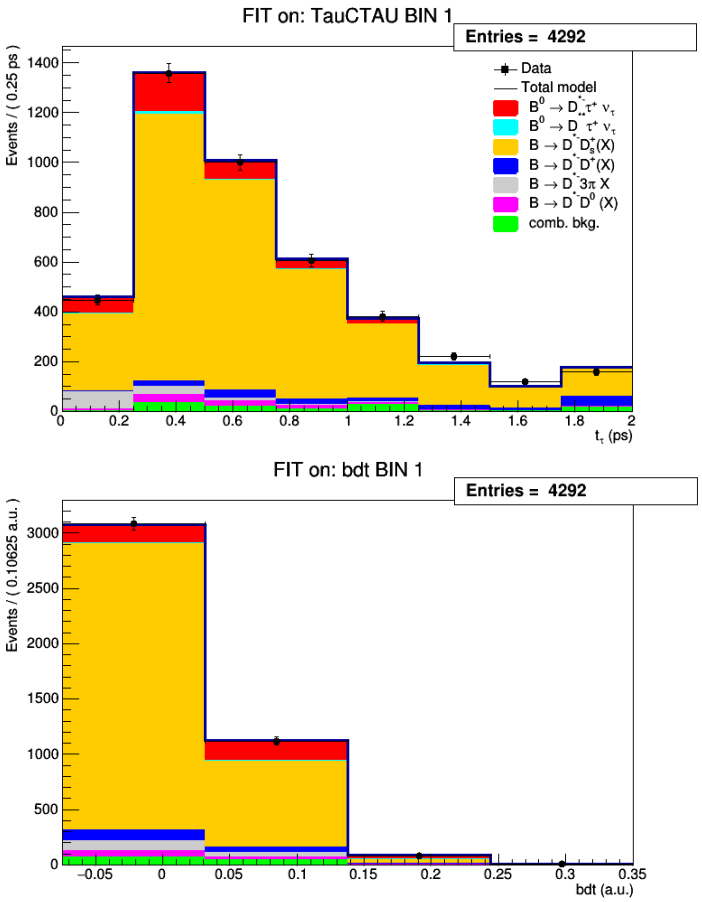

Figure 5.3: Projections of the two-dimensional fit on the (top) τ^+ decay time and (bottom) BDT output distributions n the q^2 bin: $0 < q^2 < 5.5$ GeV^2/c^4. Legend identifies the various components.

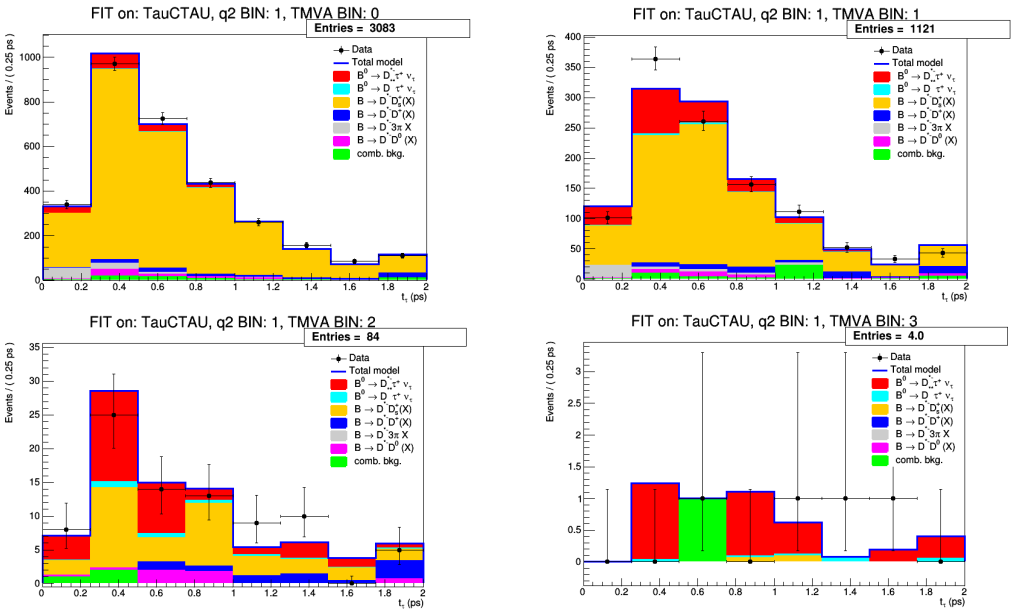

Figure 5.4: Projections of the two-dimensional model on the τ^+ decay time for the four BDT bins in the q^2 bin: $0 < q^2 < 5.5$ GeV^2/c^4. The highest BDT bin is associated to the lower-right plot.

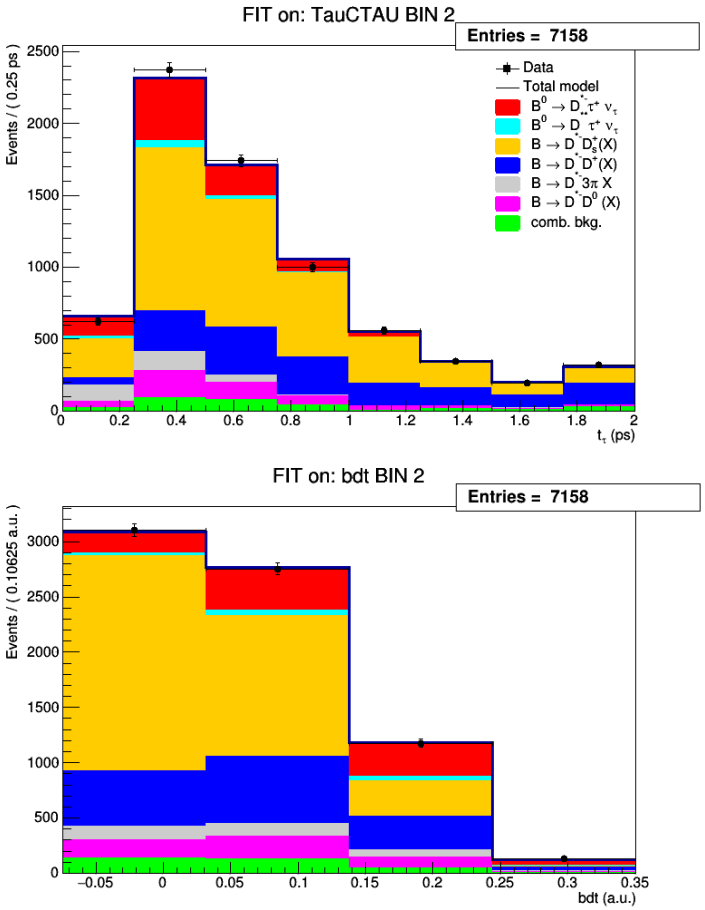

Figure 5.5: Projections of the two-dimensional fit on the (top) τ^+ decay time and (bottom) BDT output distributions n the q^2 bin: $5.5 < q^2 < 11$ GeV^2/c^4. Legend identifies the various components.

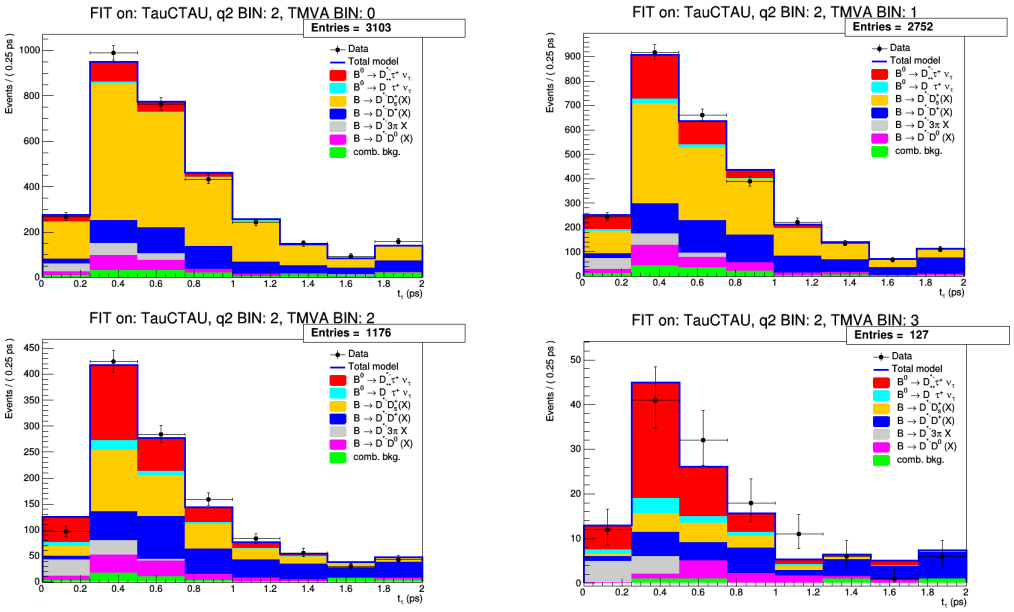

Figure 5.6: Projections of the two-dimensional model on the τ^+ decay time for the four BDT bins in the q^2 bin: $5.5 < q^2 < 11$ GeV^2/c^4. The highest BDT bin is associated to the lower-right plot.

	q^2	t_τ	BDT	BDTG
q^2	1			
t_τ	-0.06	1		
BDT	0.44	0.012	1	
BDTG	-0.07	-0.03	0.52	1

Table 5.4: Correlations between variables.

5.3 A new MVA Classifier.

As a consequence of observation (b), we are allowed to construct the templates in the way proposed in the previous section, only if we assume negligible correlations between q^2 and the fit observables, t_τ and BDT. The linear correlation coefficients for this variables can be estimated using signal MC; the results are reported in Tab. 5.4. The table tells us that the BDT distribution used so far is not suitable for a analysis in q^2 bins. Therefore, we trained a new MVA classifier: a Gradient-BDT, or BDTG [40]. Its input variables are just four:

- the minimum of the invariant mass of oppositely-charged pions, $\min[m(\pi^+\pi^-)]$,
- the maximum of the invariant mass of oppositely-charged pions, $\max[m(\pi^+\pi^-)]$
- the invariant mass of the 3π system, $m(3\pi)$
- $\frac{\texttt{tau\_PT}}{\texttt{tau\_PT+tau\_0.40\_nc\_vPT}}$, where: tau_PT is the transverse momentum of the 3π system and tau_0.40_nc_vPT is the sum of the neutral energy contained in a pseudocone of 0.4 units in $\Delta\eta - \Delta\phi$, centred around the 3π vector.

FThis new classifier was trained with the same MC samples used to create the templates of signal and D_+^s double-charm background. The complete final selection was applied. Once more, the $\tau^+ \to 3\pi\pi^0\bar{\nu}_\tau$ signal component was not exploited, for the same reasons as before. Fig. 5.7 presents the normalized and superimposed distributions of training and overtraining-test samples. The correlation coefficients between the new MVA output variable (BDTG) and the three variables, already used to fit the data, are reported in the last line of Tab. 5.4 (again signal MC was used). As wanted we get now low correlation with q^2.

5.4 Fit with the new MVA Classifier

3D Fit. We can now try to fit the data using the distributions of q^2, t_τ and BDTG. First of all, in fact, we want to check whether the new input variable permits to replicate the

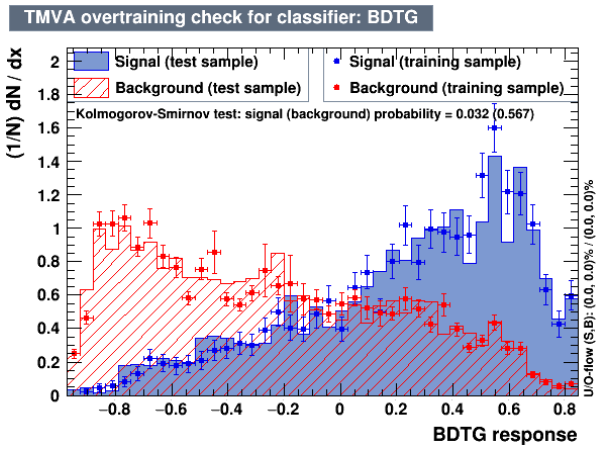

Figure 5.7: Overtraining check for the BDTG. Normalized training and test samples are superimposed both for signal and background.

published one. In order to get results directly comparable, we are going to fit data with no change in their selection. Besides, it will avoid to change the mean values of constrained and fixed parameters, which depend on the selection efficiencies. We underline that the final selection still contains the requirement on the "old" MVA classifier: $\texttt{BDT} > -0.075$. This is only necessary to have exactly the same input number of events as in the published analysis.

Concerning the fit model, nothing changes with respect to §4.6, except that the variable `BDT` is substituted by `BDTG`. Fit results are listed in the last column of Tab. 5.1, which compares them with the previous ones. Fig. 5.8 and Fig. 5.9 show the model fitted to data. The signal yield results is:

$$N_{sig}^{\texttt{BDTG}} = 1560 \pm 92, \tag{5.4}$$

to be compared to published result, $N_{sig}^{3D} = 1326 \pm 95$.

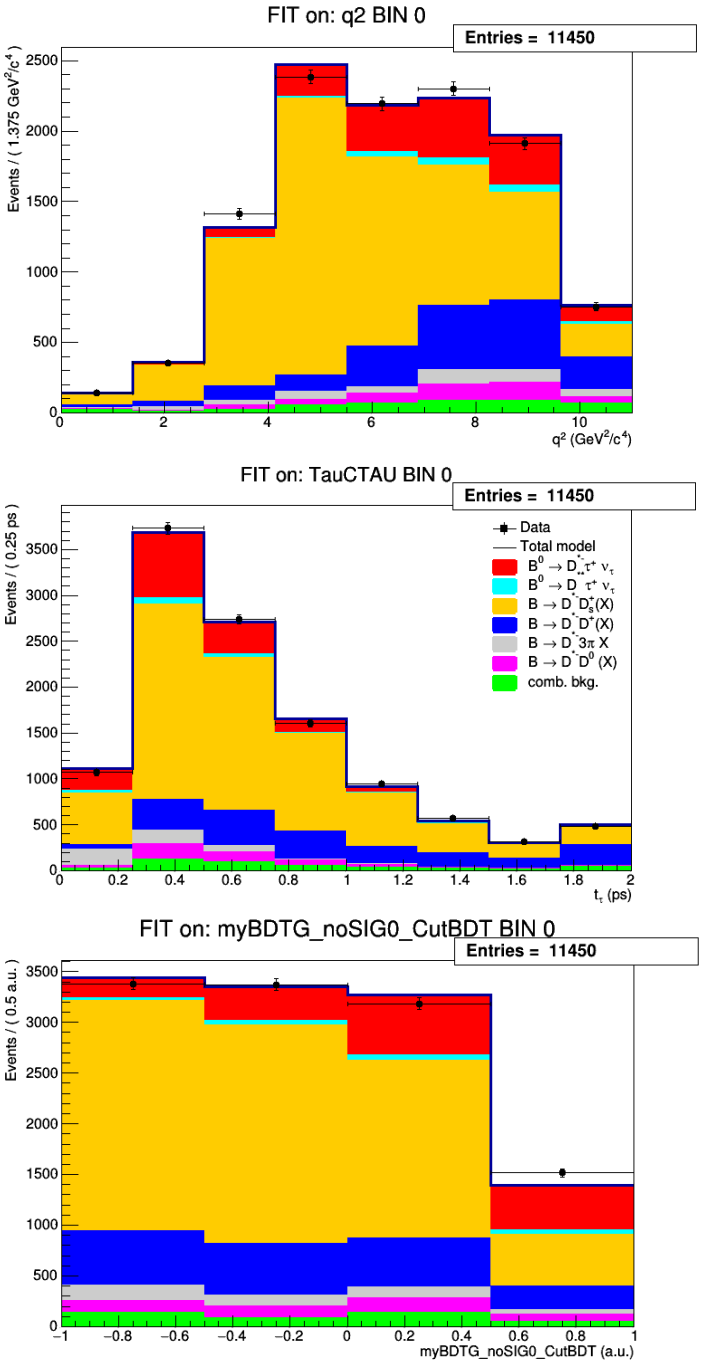

Figure 5.8: Projections of the three-dimensional fit on the (top) q^2 , (middle) τ^+ decay time and (bottom) BDTG output distributions. Legend identifies the various components.

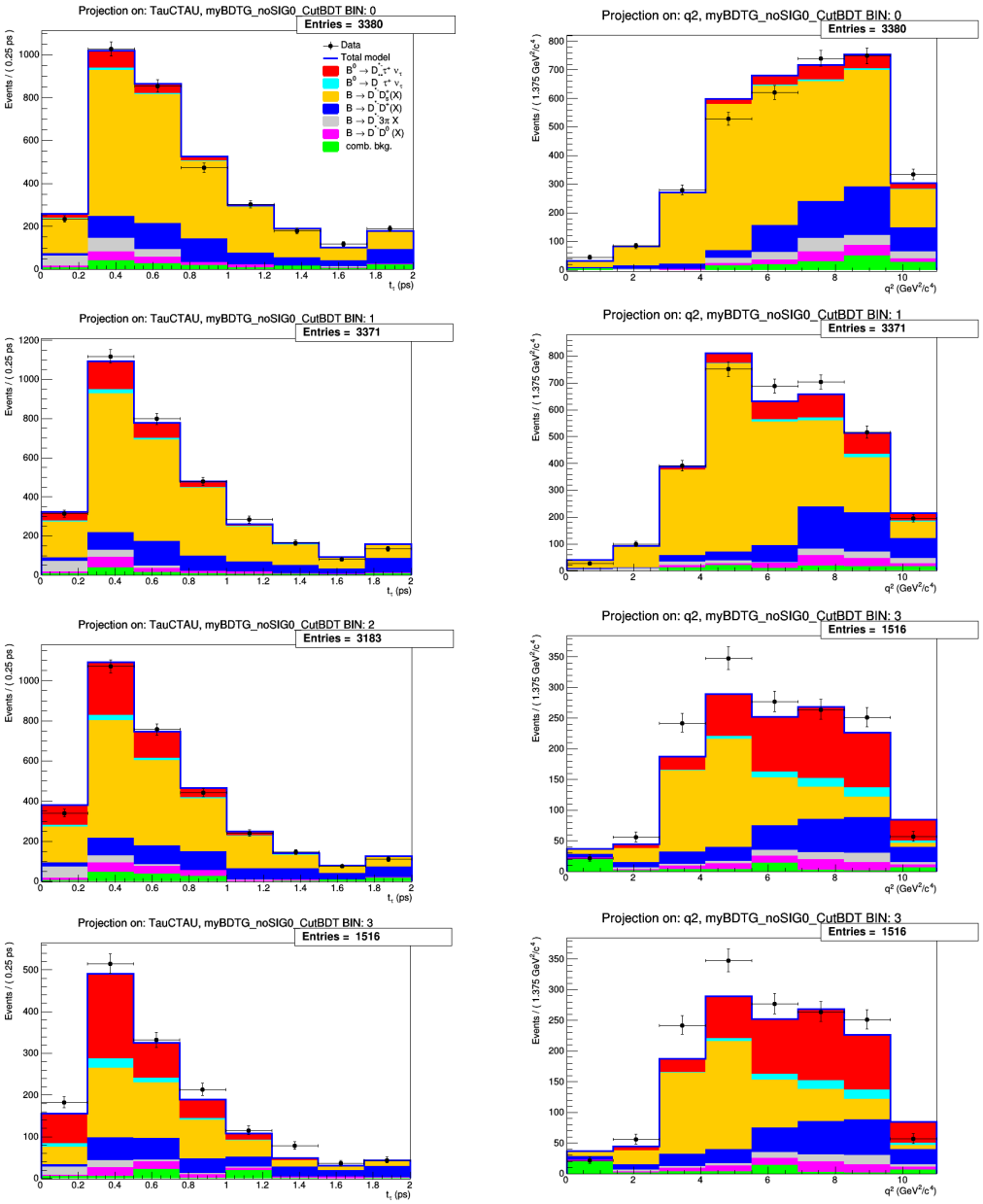

Figure 5.9: Projections on the (left) τ^+ decay time and (right) q^2 distributions for the four BDTG bins. The highest BDTG bin is associated to the two lower plots.

Chapter 6

Conclusions

The main aim of this thesis was to perform a feasibility study for the measurement of the observable R_{D^*} as function of q^2. This is performed in several steps. The first one consists to replicate the measurement of the signal yield for $B^0 \to D^{*-}\tau^+(\to 3\pi\pi^0\bar{\nu}_\tau)\nu_\tau$ decays, produced by the LHCb Collaboration [13], using Run 1 data. This steps was necessary in order to understand deeply the complexity of the fitting model to achieve the final goal of this thesis work.

The subsequent step was to demonstrate that the implemented fit model is able to discriminate signal from background, even after a q^2 marginalization. The results presented in section 5.1 confirm this hypothesis, despite an slightly enhancement of uncertainties.

After that, an extraction of the signal yield in two q^2 bins, using the two-dimensional fit model introduced in the previous step has been performed. Results consistent with the previous ones were obtained in this way.

The last step aimed to reduce what could be a main source of systematic error, *i.e.* the correlation between the `BDT` output distribution and q^2. In order to overcome this, a new multivariate analysis (`BDTG`) was implemented. Among its main features an almost uniform distribution for the sum of signal and background, which is important to reduce number of bin with low statistic in the final fit, was observed. The latter was implemented with the observables q^2, t_τ and `BDTG` in order to get results comparable to what obtained in the first test. Even if toy MC studies are necessary to conclude that the two results are not compatible, it seems that there is a discrepancy. Various hypothesis are under investigation within the LHCb working group which carry on this analysis.

Next developments for this analysis will certainly cover further tests on the BDTG distribution. First of all the enlarging of the BDTG training sample removing the selection based on the old BDT. This may reduce possible over-training problems and the observed discrepancies. A further necessary step will be to remove the selection based on the old BDT for the data sample, not only for training. To take account for this a new analysis of all selection efficiencies will be required. Finally the introduction of Run

2 data is expected to reduce by a factor 2 the statistical uncertainties. In conclusion, this work represents a fundamental step to achieve the challenging measurement of $\mathcal{R}_{D^*}$ as a function of q^2. Further studies will be necessary and will be carry on within the LHCb Bologna Group in collaboration with the LHCb CERN Group towards the final publication.

Bibliography

[1] Lees J. and al. (BaBar Collaboration). "Measurement of an excess of $\bar{B} \to D^{(*)}\tau^-\bar{\nu}_\tau$ decays and implications for charged Higgs bosons". In: *Phys. Rev. D* 88 (2013).

[2] Huschle M. and al. (Belle Colalboration). "Measurement of the branching ratio of $\bar{B} \to D^{(*)}\tau^-\bar{\nu}_\tau$ relative to $\bar{B} \to D^{(*)}l^-\bar{\nu}_l$ decays with hadronic tagging at Belle". In: *Phys. Rev. D* 92 (2015).

[3] Aaij R. and al. (LHCb Collaboration). "Measurement of the ratio of branching fractions $\mathcal{B}(\bar{B}^0 \to D^{*+}\tau^-\bar{\nu}_\tau)/\mathcal{B}(\bar{B}^0 \to D^{*+}\mu^-\bar{\nu}_\mu)$". In: *Phys. Rev. Lett.* 115 (2015).

[4] Amhis Y. and al. *Averages of b-hadron, c-hadron, and tau-lepton properties as of summer 2016*. Tech. rep. arXiv:1207.1158 [hep-ex]. Heavy Flavour Averaging Group, 2016.

[5] Fajfer S., Kamenik J., and Nisandzic I. "$B \to D^+\tau\bar{\nu}_\tau$ sensitivity to new physics". In: *Phys. Rev. D* 85 (2012).

[6] Cabibbo N. "UNITARY SYMMETRY AND LEPTONIC DECAYS". In: *Phys. Rev. Lett.* 10 (1963), p. 531.

[7] C. Patrignani et al. (Particle Data Group). "Review of Particle Physics". In: *Chin. Phys. C* 40 (2017).

[8] Buras J. "Climbing NLO and NNLO Summits of Weak Decays". In: *ArcXiv???* (2014).

[9] Aaij R. and al. (LHCb Collaboration). "Test of lepton universality using $B^+ \to K^+\ell^+\ell^-$ decays". In: *Phys. Rev. Lett.* 113 (2014).

[10] C. Bobeth and al. "Angular distributions of anti-B to K anti-l l decays". In: *JHEP 0712* 040 (2007).

[11] C. Bobeth and al. "The Decay $B^+ \to K^+\ell^+\ell^-$ at Low Hadronic Recoil and Model-Independent Delta B = 1 Constraints". In: *JHEP 1201* 107 (2010).

[12] Glashow S. L. and al. "Lepton Flavor Violation in B Decays?" In: *abc* 999 (2014), p. 999.

[13] Aaij R. and al. (LHCb Collaboration). "Measurement of the $B^0 \to D^{*-}\tau^+\nu_\tau$ branching fraction using three-prong τ decays". In: (2017). CERN-EP-2017-256, LHCB-PAPER-2017-027. arXiv: 1711.02505 [hep-ex].

[14] Nir T. "Flavor Physics and CP Violation". In: *5th Latin American School of High Energy Physics*. Recinto Quirama, Antioquia region, Colombia, Mar. 2009.

[15] Bettini A. *Introduction to Elementary Particle Physics*. II edition. Cambridge University Press, 2014.

[16] Aitchinson I. and Hey A. *Gauge Theories in Particle Physics*. IV edition. Cambridge University Press, 2014.

[17] Calibbi L. and Signorelli G. "Charged lepton flavour violation". In: *Rivista del Nuovo Cimento* 41.2 (2018).

[18] Carbone A. "Introduction to Flavour Physics (from an experimental point of view)". In: *3rd BCD-ISHEP*. Cargese, Corse, France, 2017.

[19] Braibant S., Giacomelli G., and Spurio M. *Particelle e interazioni Fondamentali*. I edition. Springer, 2009.

[20] Glashow S. L. "Partial-Symmetries of Weak Interactions". In: *Nucl. Phys.* 22 (1961), p. 579.

[21] Weinberg S. "A Model of Leptons". In: *Phys. Rev. Lett.* 19 (1967), p. 1264.

[22] Salam A. "Relativistic groups and analyticity". In: *Elemntary Particle Physics*. Ed. by Svartholm N. Stockholm: Almquvist and Wiksell, 1968.

[23] Peskin M. and Schroeder D. *An Introduction to Quantum Field Theory*. Westview Press, 1995.

[24] F. Englert and R. Brout. "Broken Symmetry and the Mass of Gauge Vector Mesons". In: *Physical Review Letters* 13 (Aug. 1964), pp. 321–323. DOI: 10.1103/PhysRevLett.13.321.

[25] P. W. Higgs. "Broken Symmetries and the Masses of Gauge Bosons". In: *Physical Review Letters* 13 (Oct. 1964), pp. 508–509. DOI: 10.1103/PhysRevLett.13.508.

[26] G. S. Guralnik, C. R. Hagen, and T. W. Kibble. "Global Conservation Laws and Massless Particles". In: *Physical Review Letters* 13 (Nov. 1964), pp. 585–587. DOI: 10.1103/PhysRevLett.13.585.

[27] T. W B Kibble. "Englert-Brout-Higgs-Guralnik-Hagen-Kibble mechanism (history)". In: *Scholarpedia* 4.1 (2009). revision #137393, p. 8741. DOI: 10.4249/scholarpedia.8741.

[28] Feinberg G and al. "Transformation of Muons into Electrons". In: *Phys. Rev. Lett.* 3 (1959). especially footnote 9, p. 527.

[29] Weinberg S. "Current Algebra and Gauge Theories. I". In: *Phys. Rev. D.* 8 (1973). especially footnote 8, p. 605.

[30] Kobayashi M. and Maskawa T. "CP-Violation in the Renormalizable Theory of Weak Interaction". In: *Progress of Theoretical Physics* 49.2 (1973), p. 652.

[31] Dassinger B. and al. "Complete Michel Parameter Analysis of inclusive semileptonic $b \to c$ transition". In: *Phys. Rev. D* 79 (2009).

[32] Faller S. and al. "Limits on New Physics from exclusive $B \to D^{(*)}\tau\bar{\nu}_\tau$ Decays". In: *Phys. Rev. D* 84 (2011).

[33] Caprini I., Lellouch L., and Neubert M. "Dispersive Bounds on the Shape of $B \to D^{(*)}l\nu$ Form Factors". In: *Nucl.Phys. B* 530 (1998), p. 153.

[34] M. Neubert. "Heavy quark effective theory". In: *34th International School of Subnuclear PhysicsâĂć*. arXiv:hep-ph/9610266. Erice, Italy, 1996.

[35] Lyndon Evans and Philip Bryant. "LHC Machine". In: *JINST* 3 (2008), S08001. DOI: 10.1088/1748-0221/3/08/S08001.

[36] B. G. Siddi. "Lepton-flavour universality tests with semi-leptonic B decays at LHCb". In: *Meeting of the APS Division of Particles and Fields (DPF 2017) Batavia, Illinois, USA, July 31-August 4, 2017*. 2017. arXiv: 1710.00369 [hep-ex].

[37] Hoecker A. and al. *TMVA 4, Toolkit for Multivariate Data Analysis with ROOT (Users Guide)*. Oct. 2013. URL: http://tmva.sourceforge.net/.

[38] Bernlochner B. and Ligeti Z. "Semileptonic $B_{(s)}$ decays to excited charmed mesons with e, μ, τ and searching for new physics with $R(D^{**})$". In: *Phys. Rev.* D95.1 (2017), p. 014022. DOI: 10.1103/PhysRevD.95.014022. arXiv: 1606.09300 [hep-ph].

[39] Betti F. and al. "Measurement of $\mathcal{B}(B^0 \to D^{*-}\tau^+\nu_t au)$ and $R(D^*)$ with τ three-prong pionic decays". (LHCb Analysis Note). May 2017.

[40] Breiman L. *Prediction Games and Arcing Algorithms*. Tech. rep. 504. Statistics Department, University of California, 1999.